TCF4 trinucleotide repeat expansions and UV irradiation are associated with ferroptosis susceptibility in Fuchs endothelial corneal dystrophy

Sanjib Saha[1], Jessica M. Skeie[2,3], Gregory A. Schmidt[3], Tim Eggleston[3], Hanna Shevalye[3], Christopher S. Sales[2,3], Pornpoj Phruttiwanichakun[1], Matthew Field[2], Tommy A. Rinkoski[4], Michael P. Fautsch[4], Keith H. Baratz[4], Madhuparna Roy[5], Albert S. Jun[5], Aliasger K. Salem[1*], and Mark A. Greiner[1,2,3*]

[1]Department of Pharmaceutical Sciences and Experimental Therapeutics, College of Pharmacy, University of Iowa, Iowa City, IA 52242

[2]Department of Ophthalmology and Visual Sciences, Carver College of Medicine, University of Iowa, Iowa City, IA 52242

[3]Iowa Lions Eye Bank, Coralville, IA 52241

[4]Department of Ophthalmology, 200 1st St SW, Mayo Clinic, Rochester, MN, 55905, USA

[5]Wilmer Eye Institute, Johns Hopkins Medical Institutions, Baltimore, Maryland 21287, USA

*Corresponding authors: mark-greiner@uiowa.edu; aliasger-salem@uiowa.edu

ABSTRACT

Fuchs endothelial corneal dystrophy (FECD), a progressive polygenic disease that causes degeneration of the corneal endothelium, is the leading indication for corneal transplantation in the U.S. Characteristically, loss of corneal endothelial cells and formation of degenerative extracellular "guttae" result in failure to maintain appropriate corneal hydration through active ion pumping to counter the passive leakage of aqueous humor. FECD pathogenesis is linked to oxidative stress and environmental exposure to ultraviolet A (UVA), and impaired endogenous response to oxidative stress is common to the disease across multiple genotypes. UV irradiation is also known to cause cellular damage by ferroptosis, a nonapoptotic oxidative cell death resulting from iron-mediated lipid peroxidation. Although a possible role for ferroptosis in FECD has been postulated to account for the increased susceptibility to oxidative damage and lipid peroxidation, this has not been explored systematically. In this study, we investigated the roles of genetic background and UVA exposure in causing lipid membrane damage and endothelial cell degeneration in FECD. We first sought clinical evidence of iron-mediated lipid peroxidation in surgical samples obtained from FECD patients undergoing endothelial keratoplasty, and found increased levels of cytosolic ferrous iron (Fe^{2+}) and evidence of lipid peroxidation were present in end-stage diseased tissues compared with healthy human donor corneas. Next, using immortalized (F35T) and primary cell cultures modeling the *TCF4* intronic trinucleotide repeat expansion genotype, we found that alterations in gene and protein expression involved in ferroptosis were conserved in both cell culture and tissue models of FECD disease compared to controls, including elevated levels of the ferroptosis-specific marker transferrin receptor 1. F35T immortalized cells showed significantly higher basal lipid peroxidation than control HCEC-B4G12 cells, indicating higher susceptibility to ferroptosis attributable to genetic background. Then, we tested the impact of physiologically relevant doses of UVA irradiation on F35T cell cultures and found increased

cytosolic Fe^{2+} iron levels indicating a role for ferroptosis in FECD disease progression. Finally, we tested the effects of inhibitory ferroptosis molecules. We found that F35T cells were more prone to RSL3 induced ferroptosis than healthy controls with deferoxamine chelation which indicated increased susceptibility in FECD cells, and cell death could be prevented after experimentally-induced ferroptosis using solubilized antioxidant ubiquinol indicating a role for anti-ferroptosis therapies. This investigation demonstrates that FECD genetic background and UVA exposure contribute to basal and incidental iron-mediated lipid peroxidation and cell death in FECD, and provides the basis for future investigations of ferroptosis-mediated oxidative damage and disease progression in FECD.

KEYWORDS: Fuchs endothelial corneal dystrophy, transferrin, ferrous iron, ferritin, ferroptosis, corneal endothelium, reactive oxygen species, ubiquinol, ultraviolet light

INTRODUCTION

Fuchs endothelial corneal dystrophy (FECD) is a complex age-related polygenic disease that affects roughly 6.1 million Americans (1) and represents the leading indication for corneal transplant surgery in the U.S. (2-6). Although this condition can be diagnosed early before it causes visual dysfunction, FECD results in surgery to restore sight because affected cells do not regenerate effectively (7) and no available medical therapy can yet prevent disease progression. In all cases, FECD is diagnosed by detecting the loss of corneal endothelial cells (CECs) and formation of degenerative extracellular matrix deposits (guttae) on the corneal endothelium that lines the inner cornea, and results in failure to maintain appropriate corneal hydration through active ion pumping to counter the passive leakage of aqueous humor (8). On the molecular level in FECD, affected CECs have an increased steady-state level of reactive oxygen species (ROS), impaired antioxidant response to oxidative stress, and increased

sensitivity to known exogenous stressors that drive disease progression including ultraviolet light (UV) (9-12). The cornea is particularly susceptible to damage by ultraviolet A light (UVA, 320 to 400 nm), which comprises the vast majority of incident solar radiation absorbed by CECs (9, 10, 13). Unlike ultraviolet B (UVB) light that causes DNA damage directly, UVA light causes macromolecular damage indirectly via the production of ROS that results from irradiation (14). DNA damage and apoptotic cell death in particular have been the focus of studies examining UV mediated cell death in FECD (9, 15-17). However, UVA is also known to result in lipid peroxidation and nonapoptotic oxidative cell death (18, 19). The roles of genetic background and UVA exposure in causing lipid membrane damage and endothelial cell degeneration in FECD have not been explored systematically. Specifically, the background effects of FECD mutation and exposure related effects of UVA irradiation on lipid peroxidation and CEC functioning in FECD patients or in vivo models have not been characterized.

A key characteristic of FECD is impaired endogenous response to oxidative stress. Vulnerability to oxidative damage in FECD has been well established, and factors that increase CEC susceptibility to lipid peroxidation have been described. Previous studies have reported decreased transcription of key antioxidant defenses in FECD including glutathione S-transferase, superoxide dismutase 2, aldehyde dehydrogenase 3A1, heme oxygenase 1, thioredoxin reductase 1, and several peroxiredoxins including Prdx 1, which protects against lipid peroxidation (20-24). Importantly, protein levels of nuclear factor erythroid 2–related factor 2 (Nrf2) – the regulator of a wide-ranging metabolic response to oxidative stress, including the cystine/glutamate antiporter (system x_c^-) that imports cysteine for glutathione biosynthesis – are reduced in FECD (20, 25). Normal levels of glutathione (GSH) and normal functioning of peroxidase 4 (GPX4), which catalyzes the reduction of lipid peroxides in a GSH-dependent reaction, are important for protecting cells against nonapoptotic oxidative cell death

via ferroptosis (26, 27). Of note, GPX4 levels are lower than controls in FECD surgical samples, indicating strongly that FECD increases susceptibility to ferroptosis (28, 29). A possible role for ferroptosis in FECD has been postulated to account for the increased susceptibility to oxidative damage and lipid peroxidation (4, 30). In addition to increased ROS-mediated lipid peroxidation and decreased GPX4 functioning, altered iron metabolism is required for ferroptosis to occur (31, 32). In health, ferric iron (Fe^{3+}) is bound to transferrin, imported into the cell via transferrin receptor 1 (TFR1, also known as CD71) mediated endocytosis, and stored in ferritin (33, 34). A pool of labile and biologically reactive Fe^{2+} is available, but levels are carefully regulated in the cell (34, 35). In pathological exposures to oxidative stress, an excess of free Fe^{2+} reacts with membrane-bound lipids to cause ferroptosis (31). Reactive Fe^{2+} at or near cell membranes can drive Fenton reactions, which cause the formation of toxic prooxidant radicals (unstable) and non-radical lipid hydroperoxide intermediaries (stable and detectable) and result in membrane-bound lipid peroxidation (36-40). This is of particular interest in FECD given the increased susceptibility to UVA-induced damage in affected patients. UV exposure is known to result in iron accumulation and ferroptosis (41-43), and iron release from ferritin with UVA irradiation have been well reported in literature (42, 44, 45). To date, no studies characterizing the role of iron, iron-lipid perturbations, or ferroptosis in FECD pathobiology have been reported.

In this study, we examined ungenotyped FECD patient surgical samples and utilized a variety of primary and immortalized cell culture models from FECD patients with pathological expansions of trinucleotide repeats in intron 3 of the *TCF4* gene (the most common genotype that causes a late onset of disease) to characterize lipid peroxidation and key iron metabolites in FECD and determine whether ferroptosis plays a role in its pathogenesis (46-48). Additionally, we compared changes in iron-lipid interactions that were attributable to genetic

background and UVA irradiation against healthy controls, and tested the effects of ferroptosis suppressor molecules. We found clear evidence of elevated lipid peroxide and cytosolic Fe^{2+} levels in FECD samples and models, consistent with increased susceptibility to ferroptosis in FECD attributable to genetic background. We identified the involvement of Fe^{2+}, a key mediator of reactive oxidation reactions, in gene-dependent susceptibility to UVA exposure and detected increases in both cytosolic and mitochondrial Fe^{2+} levels after irradiation. TFR1, which has been proposed as a specific ferroptosis marker because it is responsible for the influx of iron inside the cell (33), was found to be elevated in all samples and models and may be a useful biomarker of ferroptosis in this disease. Interestingly, of the inhibitory ferroptosis molecules tested (N-acetyl-L-cysteine as a GSH precursor, deferoxamine as a chelator, ubiquinol as an antioxidant), only solubilized ubiquinol was found to prevent cell death after experimentally induced ferroptosis in this series. Taken altogether, this study presents the first lines of evidence that iron-mediated lipid peroxidation is linked cell death in FECD, and establishes a basis for future mechanistic investigations of ferroptosis prevention in FECD.

MATERIALS AND METHODS

Consent and tissue collection

All investigations at the University of Iowa and Mayo Clinic were carried out following the guidelines of the Declaration of Helsinki. All tissues were obtained with informed consent by patients or the donor's family or next of kin. Approval was not required for the deidentified donor corneal tissues in this investigation according to the Institutional Review Board (IRB) at the University of Iowa. For FECD samples, human corneal endothelial tissue was collected at the University of Iowa and Mayo Clinic at the time of endothelial keratoplasty from patients with advanced FECD that were enrolled in the Proteomic Analysis of Corneal Health Study (IRB 201603746) or Mayo Clinic Hereditary Eye Disease Study (IRB 06-007210),

respectively. For control samples, human corneal endothelial tissue was obtained from human donor eyes provided by the Iowa Lions Eye Bank (ILEB, Coralville, IA) and Lions Gift of Sight Eye Bank (St. Paul, MN).

Materials

All required chemicals were procured from commercial sources and utilized without further purification process following the manufacturer's guidelines. Ubiquinol was procured from Sigma Aldrich (United States Pharmacopeia [USP] reference standard, USA). γ-cyclodextrin was purchased from CI America (Portland, OR). BODIPY™ 581/591 C11 lipid fluorescent probe, Dihydroethidium (Hydroethidine) and SYTOX® Green nucleic acid stain dye were procured from ThermoFisher Scientific (Invitrogen, Waltham, MA). Cytosolic ferrous iron (Fe^{2+}) detection dye FerroOrange and mitochondrial ferrous iron (Fe^{2+}) detection dye Mito-FerroGreen were purchased from Dojindo EU GmbH (Munich, Germany). LipidSpot™ 610 Lipid Droplet Stain was procured from Biotium, Inc., USA. All other solvents and reagents were analytical and cell culture grades.

Human corneal endothelial cell (HCEC-B4G12) and F35T cell culture

Healthy immortalized human corneal endothelial cells (HCEC-B4G12) were procured from Leibniz Institute DSMZ-German Collection of Microorganisms and Cell Culture GmbH, Germany, and FECD immortalized human corneal endothelial cells (F35T) were a generous gift of Dr. Albert Jun (Johns Hopkins University, Baltimore, MD). F35T cells were derived from a FECD patient expressing the *TCF4* transcript with around 4500 CUG repeats in intron 3. Both cell lines were cultured in Opti-MEM® I Reduced-Serum Medium (ThermoFisher) supplemented with 5 ng/mL of human epidermal growth factor (hEGF, ThermoFisher), 20 ng/mL of nerve growth factor (NGF, Fisher Scientific), 200 mg/L of calcium chloride (Sigma-

Aldrich), 50 µg/mL of gentamicin (ThermoFisher), 1 mL of Normocin™ (50 mg/mL, Invivogen), 0.08% chondroitin sulfate (Sigma-Aldrich) and 8% fetal bovine serum (HyClone Characterized, US origin). Media was filtered with 0.22 µM PTFE filters. Cells were incubated at 37°C with a continuous supply of 5% CO_2 and passaged at the confluence. Plastic surfaces of cell culture dishes were coated with commercial FNC Coating Mix (Athena Environmental Sciences, Inc., USA) to facilitate the adherence of endothelial cells.

Patient derived TCF4 FECD primary cell cultures

Primary HCECs were established as described previously (49). Briefly, FECD and control corneal endothelium was placed in Opti-MEM (Gibco, Waltham MA) with 8% fetal bovine serum (FBS; Gibco) overnight at 37°C, dissociated with 0.02% EDTA (Sigma, St Louis, MO) in phosphate buffered saline (PBS, Gibco) for 1h at 37°C, and plated in a single well of a 6-well collagen IV-coated plate (Corning, Tewksbury, MA) containing Joyce's medium (50). Once cell proliferation reached approximately 70%, cells were dislodged from the plate with 1X trypsin, isolated, and centrifuged at 500 g for 5 min. Pelleted cells were resuspended in Joyce's media and replated at a ratio of 1:3. HCECs were grown to confluence in Joyce's media (5-7 days) and then incubated in maturation medium (human endothelial-SFM, 2% FBS and 1X antibiotic/antimycotic) for 12 days prior to experimentation.

Human Donor and Surgical Tissue Samples

Human donor corneas were procured within 24 hours of donor death and preserved in Optisol-GS storage media (Bausch & Lomb, Irvine, CA) at 4°C. Experiments were conducted within 14 days of preservation. All donors were 50 to 75 years old and each cornea was inspected and evaluated following standard protocols and procedures of the Eye Bank Association of America (EBAA) and ILEB. Endothelial cell-Descemet membrane (EDM) tissues were

prepared by mounting donor corneas onto a 9.5 mm vacuum trephine (Barron Precision Instruments, LLC, MI, USA) and scoring the endothelium and Descemet membrane into the stroma. The ECD complex was visualized with 0.06% trypan blue ophthalmic solution (VisionBlue, DORC International, Netherlands) and the tissue was carefully peeled away from the stroma and stored at -80°C until further processing. Human corneal endothelial tissues were collected at the time of endothelial keratoplasty from patients with advanced FECD using standard surgical techniques. Immediately after removal from the eye, approximately 2/3rd of the excised tissue was placed in a cryopreservation vial on dry ice and stored at -80°C until further processing. The remaining 1/3rd of the excised tissue was sent in formalin for histopathological analysis to confirm the diagnosis of FECD.

Western blot analysis

HCEC-B4G12 (n = 5) and F35T (n = 5) cells were pelleted, and protein lysates were extracted using RIPA buffer on ice for 45 min. 0.6 µg of total protein was loaded per capillary (cat#, Protein Simple) and lysates were probed with antibodies directed at 4-HNE (STA-035, Cell Biolabs), GPX4 (MAB5457-SP, R&D Systems), SOD2 (PA5-85181, Invitrogen), NRF2 (PA5-14144, Invitrogen), FSP-1 (20886-1-AP, Proteintech), Ferroportin/SLC40A1 (PA5-G4232, Invitrogen) and TFR1 (MABS1982, Millipore) proteins. Protein expression was normalized to total protein (Cat# DM-TP01, Protein Simple) and compared between cell types.

Human FECD patient tissues samples (n = 24 pulled into groups of 3) and donor cornea EDM complexes (n = 12 pulled into groups of 3) were lysed in RIPA buffer in pools of 3 tissues for 45 minutes on ice. 0.6 µg of total protein was loaded per capillary (DM-TP01, Protein Simple) and lysates were probed with antibodies. Protein expression was normalized to total protein (DM-TP01, Protein Simple) and compared between cell types.

Real time PCR analysis

HCEC-B4G12 (n = 9) and F35T (n = 6) cells were pelleted and RNA was extracted and purified using RNeasy kit (Qiagen) according to manufacturer's instructions. 18 ng total RNA was reverse transcribed using High-Capacity cDNA Reverse Transcription kit (Applied Biosystems). qPCR was performed on the CFX Connect thermal cycler (Bio-Rad Laboratories, Inc) with 10 sec melting, 30 sec annealing/extension for 40 cycles. Melt curve analysis was performed at the end of each qPCR run to verify single product formation. ΔΔCt values were calculated between cell types normalized to *18S* and statistical analysis was performed using Student's t-test. Primers used for qPCR are: *TFR1* forward, 5'-ACCATTGTCATATACCCGGTTCA-3', *TFR1* reverse, 5'-CAATAGCCCAAGTAGCCAATCAT-3'; *18S* forward, 5'-AGAGGGACAAGTGGCGTTC-3', *18S* reverse, 5'-CGCTGAGCCAGTCAGTGT-3'.

Ferroptosis RNASeq data analysis

RNA-Seq datasets of corneal endothelial samples from 47 patients with FECD and 21 donor controls were obtained from publicly available datasets (SRA Accession Numbers: PRJNA445238, PRJNA524323, PRJNA597343). Pre-symptomatic controls with *TCF4* trinucleotide repeats were excluded from the analysis (28, 29, 51). Reads were aligned and gene counts were made using STAR (52), data quality was assessed using FastQC, gene expression was normalized, batch corrected, and determined using EdgeR (53). Genes were excluded if there were less than 3 counts in 20 or more samples. Significant differences (FDR<0.05) were calculated using EdgeR. Gene Set Enrichment Analysis was conducted on known ferroptosis gene signatures (54). For the FerrDB gene signature, all genes that were ferroptosis drivers, suppressors or markers were included, which comprised of 211 expressed

genes. Heatmap and hierarchical clustering was conducted using the ComplexHeatMap, cluster, and dendextend packages in R.

Cytosolic iron (Fe^{2+}) detection in FECD surgical and control donor corneal tissues

FECD corneal tissues were collected during endothelial keratoplasty surgery at the University of Iowa. Immediately after removal from the eye, approximately 2/3rd of the excised tissue was placed in Optisol-GS® and stored at 4°C on wet ice until further processing. Healthy donor corneas stored in Optisol-GS® at 4°C were used to prepare EDM complexes as described above. Human FECD patient tissues samples (n = 7) and donor cornea EDM complexes (n = 11, cut into half and measured as two technical replicates) were digested with 0.2% collagenase type II and 0.05% hyaluronidase in reduced serum OptiMEM-I (Gibco-BRL, Grand Island, NY) media supplemented with 50 µg/mL of gentamycin for 3h at 37°C with frequent agitation on a tube rotator (model: 05-450-127, Fisher Scientific). The digestion was finally completed with 1X 0.5% trypsin-EDTA. Following the digestion, cells were filtered with a 100 µM cell strainer to get primary cell suspension. Cells were washed once with Live Imaging Solution, centrifuged, and resuspended in 100 µL of Live Imaging Solution. Cells were transferred to 24-well plate and 300 µL of 1 µmol/L FerroOrange staining solution was added. Cells were incubated for 30 min (37°C, 5% CO_2) and transferred to flow cytometer tubes. Fluorescence was measured using a flow cytometer (BD FACSCalibur™) and results were analyzed by FlowJo (BD Biosciences, USA).

Basal level of lipid peroxidation (C11-Bodipy 581/591) assay in HCEC-B4G12 and F35T cells

HCEC-B4G12 and F35T cells were cultured in T75 flasks until they reached the confluency. After detachment with trypsin, 400,000 cells were stained with 5 µM of 2 mL C11-Bodipy

581/591 fluorescent probe in Live Imaging Solution (Thermo Fisher) or kept unstained (unstained group), mixed by pipetting, and incubated in a cell culture incubator (37°C and 5% CO_2) for 20 min. After staining, the cell suspension was transferred to 15 mL Falcon tubes corresponding to wells. All 15 mL tubes were centrifuged at 230 g for 5 min, and after the stain solution was discarded the cells were resuspended in 0.6 mL of Live Imaging Solution. After cells were transferred to flow cytometer tubes, fluorescence was measured using a flow cytometer (BD FACSCalibur™) and results were analyzed by FlowJo.

Cytosolic iron (Fe^{2+}) detection by flow cytometry using FerroOrange fluorescent probe

HCEC-B4G12 and F35T cells were cultured in T75 flasks until they reached confluency. Cells were trypsinized and washed twice with 1X DPBS buffer to remove residual trypsin and serum-containing media. The cell suspension was centrifuged at 230 g for 5 min and resuspended in Live Imaging Solution (Thermo Fisher). FerroOrange staining solution of 1 μmol/L was prepared following the manufacturer's guidelines. In 24 well plates, 150,000 cells in 100 μL Live Imaging Solution were added to each well (n = 3) and 300 μL of 1 μmol/L FerroOrange staining solution was added. For the control group, 300 μL of Live Imaging Solution was added to the cells (n = 3). Then cells were incubated for 30 min (37°C, 5% CO_2). After the incubation, cells were transferred to flow cytometry tubes and fluorescence was measured by flow cytometry (BD FACSCalibur™). Data analysis was carried out using FlowJo software.

Mitochondrial iron (Fe^{2+}) detection by flow cytometry using Mito-FerroGreen fluorescent probe

HCEC-B4G12 and F35T cells were cultured, trypsinized, washed, and resuspended in Live Imaging Solution following the same protocol as cytosolic iron detection. Mito-FerroGreen staining solution of 5 μmol/L was prepared following the manufacturer's guidelines. For the

experimental group, 500 µL of 5 µmol/L Mito-FerroGreen staining solution was added to 150,000 cells in 100 µL of Live Imaging Solution in 24-well plate (n = 3). For the control group, 500 µL of Live Imaging Solution was added to the cells (n = 3). After the incubation of 30 min (37°C, 5% CO_2), fluorescence was measured using a flow cytometer (BD FACSCalibur™) and data was analyzed by FlowJo.

Basal level of lipid droplets quantification

HCEC-B4G12 and F35T cells at 250,000 cells/well in 24-well plate were stained with 1X of LipidSpot™ 610 in 1 mL of cell culture media and incubated for 30 min (37°C, 5% CO_2). After incubation cells were transferred to flow cytometer tubes. Fluorescence was measured using a flow cytometer (BD FACSCalibur) and data was analyzed by FlowJo.

Confocal microscopy

Confocal microscopy was conducted with multiple fluorescent probes, including C11-Bodipy 581/591 fluorescent probe for imaging lipid peroxidation, FerroOrange for cytosolic labile iron, Mito-FerroGreen for mitochondrial iron, Dihydroethidium (Hydroethidine) for ROS, and LipidSpot™ 610 for lipid droplets. HCEC-B4G12 and F35T cells were seeded at 100,000 to 200,000 cells/chamber in 4-chambered coverglass (Thermo Scientific Nunc Lab-Tek) after coating the glass surface with FNC Coating Mix and incubated at 37°C and 5% CO_2. After 18 to 72 h, media was discarded, and cells were washed with Live Imaging Solution if required according to manufacturer depending on the fluorescent probe used in experiment. For iron detection, washing at least twice was important to remove extracellular iron from the media. For lipid peroxidation imaging, cells were stained with 0.9 mL of 5 µM C11-Bodipy 581/591 fluorescent probe in Live Imaging Solution for 20 min and stain solution was discarded before adding 0.9 mL of fresh Live Imaging Solution. For cytosolic and mitochondrial iron imaging,

after washing twice, 500 µL of 1 µmol/L FerroOrange and 5 µmol/L Mito-FerroGreen staining solutions were added to the cells and incubated for 30 min. For ROS imaging, cells were stained with 0.9 mL of 10 µM Dihydroethidium fluorescent probe in Live Imaging Solution for 30 min. For lipid droplet imaging, cells were stained with 0.9 mL of 1X LipidSpot™ 610 fluorescent probe in cell culture media for 30 min. All incubation was conducted in cell culture incubator at 37°C and 5% CO_2. Immediately after incubation, live cells were imaged by Leica SP8 confocal microscope with 63X oil lens. For each dye, all images were taken at the same gain level and image capture settings for both HCEC-B4G12 and F35T cells. The operating software was Leica Application Suite X (LAS X). Images were analyzed using Image J.

Deferoxamine (DFO) iron chelation assay

HCEC-B4G12 and F35T cells were seeded in 96-well plates at 5,000 cells/well. After 18 h of incubation at 37°C and a continuous supply of 5% CO_2, cells were treated with 100 µM of DFO (n = 3). After the incubation of 24nh (37°C and 5% CO_2), cells were washed once with 1X DPBS, and RSL3 at the doses of 1, 2, and 5 µM in DMSO were added to the respective cells while an equal amount of DMSO was added to the control cells, and incubated for 2, 4, 6 and 8 h (37°C and 5% CO_2). After the RSL3 treatment of 2, 4, 6, and 8 h, at each time point, cells were gently washed once with 1X DPBS and MTS reagent of 20 µL (Cell Titer-96 Aqueous One Solution, Promega, USA) in 80 µL of cell culture media was added to the cells and incubated for 3 h (37°C and 5% CO_2). After the incubation, the absorbance was measured at 490 nm using the Spectra Max plus 384 Microplate Spectrophotometer (Molecular Devices, Sunnyvale, CA) following the manufacturer's guidelines.

Cytosolic ferritin ELISA

HCEC-B4G12 and F35T cells were cultured in T75 flasks with 3 biological replicates. At confluence, the protein was extracted with 1X RIPA buffer (Sigma-Aldrich) supplied with EDTA-free Protease Inhibitor Cocktail (cOmplete™, Roche). Protein was stored at -80°C until the ELISA assay was performed. Protein concentration in each biological replicate was measured by Pierce™ BCA Protein Assay Kit (Thermo Scientific™). Three technical replicates of 100 µg protein from each biological replicate diluted with diluent supplied by the manufacturer were added to the antibody-coated wells (Ferritin Human ELISA Kit, Invitrogen). All the steps were carried out following the manufacturer's protocol. Spectra Max plus 384 Microplate Spectrophotometer was used to measure the absorbance at 490 nm. The standard calibration curve of ferritin was prepared in duplicates.

Mitochondrial ferritin (MTFT) ELISA

Mitochondrial ferritin in HCEC-B4G12 and F35T cells were quantified using Immunotag™ Mitochondrial Ferritin ELISA kit (G-Biosciences, USA). Protein was extracted following the same protocol mentioned above in cytosolic ferritin ELISA. Three technical replicates of 100 µg protein from each biological replicate (n = 3) were added to antibody-coated wells and all the experimental steps were conducted according to the manufacturer's guidelines without any modification. The standard calibration curve of FTMT was prepared in duplicates.

Mitochondrial superoxide assay

HCEC-B4G12 (n = 12) and F35T (n = 8) cells (50,000/well and 25,000/well, respectively) were grown in 96 well plates until reaching confluency. Cells were exposed to MitoROS 580 dye (ab219943, Abcam) for 30 min, and mitochondrial superoxide was quantified using Infinite M Plex plate reader (Tecan Group, Ltd) with Ex/Em =540/590 nm. Cells were fixed with 4% formaldehyde buffered in 0.1 M PBS, pH 7.4 for 30 min, washed with PBS 3 times, and

incubated with 300 nM DAPI for 30 min. DAPI-stained nuclei were counted in whole well images captured by Cytation 5 instrument (BioTek Instruments, Inc) using Gen5 Image Plus (version 3.10) software, and resulting cell counts were applied to obtain normalized MitoROS 580 RFU/cell values for each well. Average values were calculated per group and compared. As a positive assay control, additional B4G12 and F35T cells were treated with antimycin-A (AMA) for 30 min prior to and during the MitoROS 580 dye treatment, for a total of 60 min.

Basal level of ROS quantification

HCEC-B4G12 and F35T cells at 250,000 cells/well in 24-well plate were stained with 10 µM of dihydroethidium (DHE) in 1 mL of Live Imaging Solution and incubated for 30 min (37°C, 5% CO_2). After incubation cells were transferred to flow cytometer tubes. Fluorescence was measured using a flow cytometer (BD FACSCalibur) and data was analyzed using FlowJo.

Multidimensional protein identification technology (MudPIT) mass spectrometry

Aqueous humor samples from patients with FECD (n = 4) and patients without FECD (n = 4) were collected. The filter-assisted sample preparation (FASP) method was used for preparing samples for digestion (55). It was solubilized in a mix containing ionic detergent 5% sodium deoxycholate (SDC), buffer 100 mM triethylammonium bicarbonate (TEAB) at pH 8.0, and 3 mM dithiothreitol (DTT). Samples were then sonicated, spun down, and finally the supernatant was transferred to a 30 kD MWCO filter (Millipore, MA, USA) and centrifuged for 30 min at 13,000 g. The filtrate was discarded, and the remaining sample was buffer exchanged with 1% SDC and 100 mM TEAB at pH 8.0. Following buffer exchange, the sample was alkylated with 15 mM iodoacetamide and then digested overnight with trypsin at an enzyme to substrate ratio of 1:100 in a Thermo-Mixer at 1000 RPM at 37°C. Peptides were collected by centrifugation and reversed-phase stop-and-go extraction (STAGE) tips were used for desalting

approximately 20 µg of digested peptides (56). Elution solvent was a mixture of 80% acetonitrile and 5% ammonium hydroxide. Desalted peptides were lyophilized in a SpeedVac (Thermo Fisher Scientific, MA, USA) for 1 h. Peptide samples were then analyzed by ultra-performance liquid chromatography coupled with tandem mass spectrometry (UPLC-MS/MS). The UPLC system was an Easy-nLC 1000 UHPLC system (Thermo Fisher Scientific) coupled with a quadrupole-Orbitrap mass spectrometer (Q-Exactive; Thermo Fisher Scientific). The column was 2 µM Thermo Easy Spray PepMap C18 column (Thermo Fisher Scientific) with 500 mm × 75 µM i.d. Two mobile phases were used, phase A was composed of 97.5% MilliQ water, 2% acetonitrile, and 0.5% formic acid and phase B was composed of 99.5% acetonitrile, and 0.5% formic acid. The elution events were 0-210 min, 0-25% B in A and 210-240 min, 25-80% B in A. Nano-electrospray ionization (Thermo Easy Spray source; Thermo Fisher Scientific) was used at 50°C with an electrospray voltage of 2.2 kV. Tandem mass spectra were acquired from the top 20 ions in the full scan in the range between 400 – 1200 m/z while dynamic exclusion was set to 15 seconds and singly-charged ions were excluded from the analysis. Isolation width was set to 1.6 Dalton and full MS and MS/MS resolution were set to 70,000 and 17,500, respectively. The normalized collision energy was 25 eV and automatic gain control was set to 2e5. Max fill MS and max fill MS/MS were set to 20 and 60 milliseconds, respectively, and the underfill ratio was set to 0.1%.

For identifying peptides, msconvert was used to convert RAW data files to mzML format (57) and then Peak Picker HiRes tool from the OpenMS framework was used to generate MGF files from mzML format (58). Peptide identification searches required precursor mass tolerance of 10 parts per million, fragment mass tolerance of 0.02 Da, strict tryptic cleavage, up to 2 missed cleavages, variable modification of methionine oxidation, fixed modification of cysteine alkylation, and protein-level expectation value scores of 0.0001 or lower. Finally, MGF files

were searched using up-to-date protein sequence libraries available from X!Tandem (59), UniProtKB, and OMSSA (60). Identified protein intensities were normalized to total peptide hits per sample and scaled to logarithmic base 10. Partek Genomics Suite version X.X. (MO, USA) was used to determine statistically significant proteins (analysis of variance [ANOVA], $P<0.05$). Pathway significance was ascertained by the number of proteins in the dataset in common with known proteins in a single pathway, as determined by the IPA database (Qiagen).

Cytosolic iron (Fe^{2+}) detection in human donor corneas upon UVA irradiation

Human donor corneas stored in Optisol-GS® at 4°C were procured as noted above. This experiment was performed in pairwise fashion, where the right eye was exposed to UVA irradiation (n = 3) and the left eye from the same donor was used as a control. Corneas were washed with sterile Hank's balanced salt solution (HBSS) and placed in 12-well plate in HBSS with endothelial side facing the UVA light source. Cells were exposed to UVA irradiation at the fluence of 5 J/cm^2 using a Rayonet Photochemical Reactor (RPR-200, The Southern NE Ultraviolet Co., Brandford, CT). Four RPR-3500A UVA broadband lamps of 12-inch length emitting 350 nm light with an irradiance of 7.13 mW/cm^2 were placed at 10 cm above the cells and illuminated for 11 min 41 sec to achieve a 5 J/cm^2 UVA dose. Initially, various UV fluence levels of 5 to 25 J/cm^2 with 5 J/cm^2 increments were screened to find a relatively safe UV dose for cells by measuring cell viability after UVA irradiation using a MTS assay kit. Control corneas were treated identically except they were not subjected to UVA irradiation. Both UVA irradiated and unexposed control corneas were digested following the same procedures noted previously and primary cell suspensions were obtained. Cells resuspended in 100 µL of Live Imaging Solution were transferred to 24-well plate and 600 µL of 1 µmol/L FerroOrange staining solution was added to each well. Staining was performed for 30 min (37°C and 5%

CO_2). Fluorescence were measured using a flow cytometer (BD FACSCalibur) and data were analyzed using FloJo.

Cytosolic and mitochondrial Iron (Fe^{2+}) detection upon UVA irradiation

HCEC-B4G12 and F35T cells were cultured and prepared following the same protocol as used for cytosolic iron detection. In order to quantify cytosolic iron, 400,000 cells in 300 µL of Live Imaging Solution were added to each well in a 24 well plate. The UVA irradiation instrument set-up was the same as noted previously for the irradiation of human corneas. Various doses of UVA irradiation of 1, 2, 4, and 8 J/cm^2 fluences were delivered. UVA irradiated and control cells were stained with 1.2 mL of 1 µmol/L FerroOrange staining solution for 30 min in the incubator (37°C, 5% CO_2). For the detection of mitochondrial iron, 20,000 cells in 200 µL of Live Imaging Solution were added to each well and irradiated with a UV dose of 5 J/cm^2. UV irradiated and control cells were stained with 700 µL of 5 µmol/L Mito-FerroGreen staining solution for 30 min in an incubator (37°C, 5% CO_2). The same volume of Live Imaging solution was added to the unstained control group, which was used to monitor background fluorescence signals. After incubation, fluorescence was measured using a flow cytometer (BD FACSCalibur) and data was analyzed by FlowJo.

Preparation of solubilized ubiquinol

Solubilized ubiquinol was prepared by kneading method where physical complexation was formed between ubiquinol and γ-cyclodextrin (γ-CD) following our previously published protocol (30). Briefly, ubiquinol and γ-CD were mixed at the molar ratio of 1:10 and a hydro-alcoholic solution at 1:1 ratio was added to the mixture to form a semi-liquid paste. Mixing was continued around 1h and vacuum dried to yield the powdered complex.

Lipid peroxidation inhibition by solubilized ubiquinol in HCEC-B4G12 and F35T cells

The lipid peroxidation assay was conducted using C11-Bodipy 581/591 fluorescent probe following the same seeding, washing, staining and measurements steps described in the basal lipid peroxidation assay, except cells were treated with solubilized ubiquinol then challenged with 1 μM of RSL3 or left untreated as controls. 18 h after seeding, media was removed and solubilized ubiquinol at concentrations of 1, 10, 50, and 100 μM in cell culture media were added to the cells (n = 3) and incubated for 24 h (37°C and 5% CO_2). After incubation, cells were washed twice with 1X DPBS, and 1 μM of RSL3 in DMSO was added except for the untreated and untreated-unstained control groups. Cells were then incubated for 8 h at 37°C and 5% CO_2, and after the incubation, cells were stained with 2 μL of C11-Bodipy 581/591 fluorescent probe stock prepared in DMSO as described in the basal lipid peroxidation assay.

Ferroptosis assay in HCEC-B4G12 and F35T cells

Lactate dehydrogenase (LDH) assay was performed using CyQUANT™ LDH Cytotoxicity Assay kit (Invitrogen, USA). LDH release in media was quantified as an endpoint of measuring ferroptosis. HCEC-B4G12 and F35T cells were seeded at 5,000 cells/well in a 96-well plate and incubated for 18 h (37°C and 5% CO_2). After incubation, media was removed, and solubilized ubiquinol dispersed in media was added at 1, 5, 10, 50, and 100 μM concentrations while only media was added to the control group. In this assay, there were two control groups: one group was used for measuring the spontaneous LDH activity, and another group was used for measuring maximum LDH activity. Ferrostatin-1 (Sigma-Aldrich, USA), a known ferroptosis inhibitor, was dissolved in DMSO at 1 μM and used as a positive control. After incubating for 24 h at 37°C and 5% CO_2, cells were washed twice with 1X DPBS and treated with 1 μM of RSL3 in DMSO whereas control groups had an equal amount of DMSO in media. After 24 h of incubation, 10 μL of supplied 10X lysis buffer was added to the group designated

for measuring the maximum LDH activity and incubated in the cell culture incubator for 45 min. Following 45 min incubation, 50 µL from each well was transferred to a new 96-well flat-bottom well plate. To test the assay performance, 50 µL of 1X LDH positive control was added to three wells which were used as the positive control group. The supplied reaction mixture of 50 µL was added and incubated for 30 min at dark at room temperature (RT). A stop solution of 50 µL was added to each well for stopping the reaction. Absorbance was measured at 490 nm following the manufacturer's protocol. Percent cell viability was calculated using the formula mentioned below:

$$\% \text{ Cell viability} = 100 - \left(\frac{\text{Compound treated LDH activity} - \text{Spontaneous LDH activity}}{\text{Maximum LDH activity} - \text{Spontaneous LDH activity}}\right) \times 100$$

Ferroptosis assay in F35T cells using MTS assay

F35T cells were seeded at 2,500 and 5,000 cells/well in 96-well plate and incubated for 18 h (37°C and 5% CO_2). After the incubation, media was removed, and solubilized ubiquinol, N-Acetylcysteine (NAC) and deferoxamine (DFO) dispersed in media were added separately at 1 and 10 µM concentrations while only media was added to the control group. Ferroptosis inhibitor ferrostatin-1 (Sigma-Aldrich, USA) in DMSO was used as a positive control. After adding treatments, cells were incubated for 24 h (37°C and 5% CO_2). Cells were then washed twice with 1X DPBS to remove any residual treatments and 1 µM of RSL3 in DMSO was added to the cells except for the no RSL3 control group where only DMSO in media was added. After adding RSL3, cells were incubated for 24 h (37°C and 5% CO_2) and bright-field microscopic images of live cells were taken using EVOS Cell Imaging System (ThermoFisher, USA). Cells were gently washed once with 1X DPBS and 20 µL of MTS reagent in 80 µL of media were added to the cells and incubated for 3 h (37°C and 5% CO_2). After the incubation, the absorbance was measured at 490 nm following the manufacturer's guidelines.

Time-lapse confocal imaging of ferroptosis

Cells were seeded at 100,000 cells/chamber in a 4-chambered glass bottom coverglass (Thermo Scientific Nunc Lab-Tek) after coating with FNC Coating Mix and incubated for 18 h (37°C and 5% CO_2). Cells were treated with 1 μM of RSL3, 1X of LipidSpot™ 610 and 50 nM of SYTOX™ Green nucleic acid stain dye in 0.9 mL of cell culture media. Time-lapse Z-stack imaging was performed up to 17 h using a LSM 980 confocal microscope (Zeiss) with Airyscan 2 with 63X oil lens. During imaging, cells were incubated in the chamber maintained at 37°C and 5% CO_2. Image analysis and video production were performed in Imaris 9.9 (Oxford Instruments).

Statistical analysis

All data were expressed as the mean ± standard error of the mean (SEM). Statistical analysis was performed using the two-tailed Student's t-test when the experimental group was only compared with the control group. One-way ANOVA followed by Tukey's post-hoc test was utilized when multiple groups were compared with each other. p-values of less than 0.05 were considered statistically significant. All experiments were carried out with at least 3 biological replicates and in technical triplicate. Statistical analysis was carried out using GraphPad Prism.

RESULTS

FECD surgical samples demonstrate key markers of ferroptosis including increased lipid peroxidation, cytosolic iron accumulation, and changes in gene and protein expression.

Endothelial cell-Descemet membrane tissue samples resected from ungenotyped FECD patients during endothelial keratoplasty were used to determine the presence of ferroptosis (excessive lipid peroxidation and elevated labile cytosolic ferrous iron [Fe^{2+}]) in end-stage

disease compared to healthy controls. First, Western blot analysis with anti-4-HNE was performed to detect lipid peroxidation in human surgical samples from FECD patients (n = 8). Surgical samples with FECD had 30% higher 4-HNE expression than control donor tissues ($p < 0.01$) (**Fig. 1A, *S1***). Higher 4-HNE expression in FECD tissues indicated higher basal level of lipid peroxidation in FECD patients. Then, the labile cytosolic iron in endothelial cells of FECD patients was quantified to determine the presence of higher iron accumulation in FECD pathophysiology. Primary corneal endothelial cells were isolated from FECD surgical tissues obtained during endothelial keratoplasty and cytosolic iron was quantified by flow cytometry and compared with isolated corneal endothelial cells from healthy human donor corneas. FECD cells had a 32.23% increase in FerroOrange fluorescence compared to healthy donor controls ($p < 0.01$), indicating a significantly higher cytosolic Fe^{2+} content in FECD (**Fig. 1B**). Of note, only cytosolic Fe^{2+} was assayed in FECD surgical tissue explants in this series because of the limited availability of tissues and scarcity of live cells in resected tissue.

Next, we probed tissue samples resected from ungenotyped FECD patients during endothelial keratoplasty that represent end-stage FECD disease and healthy donor tissue controls to determine alterations to key genes and proteins known to occur in ferroptosis. Glutathione peroxidase (GPX4) prevents lipid peroxidation and ferroptosis (61). Therefore, downregulation of *GPX4* results in disruption of redox homeostasis and significantly more lipid peroxidation, and this is a well-documented change that occurs in ferroptosis (26, 62). FECD surgical samples had 0.62-fold lower gene expression than healthy donor cornea samples ($p = 0.05$; **Fig. 1C**). Superoxide dismutase 2 (SOD2), a key antioxidant enzyme responsible for neutralizing harmful superoxide anion (O_2^{-}), is known to protect against ferroptosis (63). *SOD2* gene expression has been found to be downregulated by 0.30-fold in FECD tissues in comparison to healthy control tissues in qPCR analysis ($p < 0.01$; **Fig. 1D**). SOD2 protein

expression was also significantly lower in FECD tissues than in healthy tissues ($p < 0.05$; **Fig. 1D**). The transcription factor nuclear factor erythroid 2-related factor 2 (NRF2) is a key player in antioxidant defense and master regulator of genes responsible for preventing lipid peroxidation, iron accumulation and oxidative damage (64). *NRF2* gene expression was downregulated by 0.57-fold in FECD tissues when compared with control tissues ($p < 0.01$; **Fig. 1E**). However, NRF2 protein was significantly overexpressed in FECD tissues in comparison to healthy tissues ($p < 0.05$; **Fig. 1E**). In contrast to GPX4 which is a glutathione dependent ferroptosis inhibitor, ferroptosis suppressor protein 1 (FSP1) has been found to be a glutathione-independent ferroptosis inhibitor (65). FSP1 is known to complement the loss of GPX4 and is upregulated in ferroptosis, while GPX4 is downregulated to protect cells against ferroptosis (65). FSP1 as CoQ oxidoreductase, catalyzes the NAPDH dependent reduction of oxidized form of CoQ10, ubiquinone to the active reduced form of CoQ10, ubiquinol which protects cells from ferroptosis by inhibiting lipid peroxidation (65, 66). In this study, *FSP1* gene expression was found to be downregulated by 0.6-fold in FECD tissues in comparison to control tissues ($p < 0.05$; **Fig. 1F**). FSP1 protein expression was found to be increased by 32% in FECD surgical samples in comparison to healthy donor cornea samples in western blot analysis ($p < 0.05$; **Fig.1F**). Ferroportin (FPN1) also known as SLC40A1, is a sole iron exporter plays crucial role in maintaining iron homeostasis (67). *FPN1* gene expression was significantly upregulated by 2.06-fold in FECD tissues in comparison to control tissues ($p = 0.05$; **Fig.1G**), which indicates a compensatory response in disease to export higher labile iron and restore iron homeostasis. FPN1 protein was also significantly overexpressed by 190% in FECD tissues when compared with control tissues ($p < 0.001$; **Fig.1G**). Acyl-CoA synthetase long chain member family 4 (ACSL4), a key player in cell death including ferroptosis, is responsible for regulating lipid biosynthesis by converting fatty acid to fatty acyl-CoA esters (68, 69). *ACSL4* gene expression was downregulated by 0.46-fold in FECD tissues in

comparison to control tissues ($p < 0.05$; **Fig.1H**), which indicates cells downregulating lipid peroxidation precursors ***.

We also performed an analysis of published databases of samples from FECD patients and controls for the presence of genes known to be involved in ferroptosis. Genes involved in ferroptosis were downregulated in FECD patients compared to control patients (FDR < 0.01). Strikingly, a mixed model analysis that allows for both upregulated and downregulated genes was more significantly enriched for changes consistent with ferroptosis occurrence in FECD (FDR < 0.001, **Fig. 1I**), indicating an overall dysregulation of the ferroptosis pathway in FECD. The most significant alteration occurred in the mixed model analysis from the FerrDB database, which includes known driver, suppressor, and marker genes of ferroptosis (54).

FECD cell cultures modeling TCF4 repeat expansion recapitulate human tissue findings and demonstrate key markers of ferroptosis.

4-HNE was significantly overexpressed in FECD tissues indicating higher basal levels of lipid peroxidation, however in cell culture models we initially found no significant differences between HCEC-B4G12 and F35T cells ($p = 0.15$; **Fig. 2A, *S2***). Therefore, in our cultured cell models, we also analyzed basal levels of lipid peroxidation by quantifying differences in a fluorescent probe, C11-Bodipy 581/591, which acts as a reporter of lipid peroxidation by shifting fluorescence from red to green in response to exposure to ROS (70, 71). ROS-mediated oxidation of the polyunsaturated butadienyl part of the fluorescent probe causes the peak shift indicating the lipid peroxidation. Basal level of lipid peroxidation was quantified in both HCEC-B4G12 and F35T cells to compare the extent of lipid peroxidation without any cellular treatment. F35T cells were found to have a 2.89-fold higher basal level of lipid peroxidation when compared to HCEC-B4G12 cells ($p < 0.0001$; **Fig. 2B**). In representative confocal

images, there was notable difference in red and green fluorescence between HCEC-B4G12 and F35T cells. In HCEC-B4G12 cells, the majority of the fluorescence signal was red and came from the reduced form of the fluorescent probe, which was emitted at 591 nm. In F35T cells, oxidation of the polyunsaturated butadienyl portion of the dye shifted the emission peak from 591 nm to 510 nm, and the majority of the fluorescence signal was green (**Fig. 2C**).

Next, the cytosolic iron content was detected using a fluorescent probe to assess the availability of the toxic ferrous iron (Fe^{2+}) pool that can drive ferroptosis. Labile cytosolic Fe^{2+} has been found to be increased during ferroptosis (72). Because ferroptosis is driven by labile iron overload, we first detected cytosolic iron content and compared F35T to HCEC-B4G12 cells. FerroOrange (Dojindo EU GmbH) is a fluorescent probe capable of live-cell fluorescent staining of cytosolic Fe^{2+} iron through the formation of a stable fluorescent complex (73). In flow cytometry analyses, F35T cells were found to have 3.3-fold higher cytosolic Fe^{2+} iron detected by an increase of fluorescence compared to HCEC-B4G12 cells indicating toxic ferrous iron overload ($p < 0.0001$; **Fig. 2D**). In cell population comparisons, 60.87±1.3% of F35T cells were present in the gated region of FL2 fluorescence above the background signal of unstained cells, whereas only 36.67±3.1% of HCEC-B4G12 cells were detected in that region (**Fig. 2E**). Confocal microscopy imaging also revealed that the fluorescent intensity of FerroOrange was markedly higher in F35T cells compared to HCEC-B4G12 cells, indicating a higher amount of labile ferrous iron in F35T cells (**Fig. 2F**).

Mitochondria are key regulators of corneal endothelial cell redox signaling and antioxidant function. Iron plays a crucial role in mitochondrial function through controlling Fe-S cluster and heme protein biosynthesis, electron transport, and oxidative phosphorylation (74). Mitochondria need iron for proper functioning, but iron overload disrupts iron homeostasis and

leads to mitochondrial dysfunction, iron-dependent oxidative stress, and iron-mediated endothelial cell dysfunction (75). Herein, we quantified mitochondrial ferrous iron (Fe^{2+}) content in cells using Mito-FerroGreen, a specific fluorescent probe capable of staining mitochondrial iron content in live cells (76). The fluorescent intensity of Mito-FerroGreen was 10.9-fold higher in F35T cells than in HCEC-B4G12 cells in flow cytometry analyses, which indicated very high Fe^{2+} content in the mitochondria of F35T cells compared to healthy cells ($p < 0.0001$; **Fig. 2G**). In cell population comparisons, 6-times more F35T cells (64.33±1.17%) were present in the gated region of FL1 fluorescence above the background signal of unstained cells whereas only 10.27±0.4% B4G12 cells were detected in that region (**Fig. 2H**). Higher fluorescence intensity of Mito-FerroGreen in F35T cells than in HCEC-B4G12 cells was also detected in confocal microscopy imaging (**Fig. 2I**).

Deferoxamine (DFO) is well-known iron chelator and can inhibit the ferroptosis process by lowering cytosolic labile iron concentrations (77). Since DFO can inhibit ferroptosis, we used DFO treatment as an indirect way of assessing the susceptibility of F35T cells towards ferroptosis and comparing them with healthy HCEC-B4G12 cells (77-79). Cells were treated with RSL3, which is a known RAS-selective and lethal ferroptosis inducer (80). RSL3 inhibits GPX4 and results in the accumulation of lipid ROS and an increase in the labile iron pool, and thus induces ferroptosis in dose dependent manner (81). When cells were treated with RSL3 for 2 h at different concentrations, both cell types had a similar percentage of cell viability. Surprisingly, F35T cells had significantly higher cell death when RSL3 treatment duration was increased to 4, 6, and 8 h at all three different concentrations of 1, 2, and 5 μM ($p < 0.0001$; **Fig. 2J**). Higher cell death in F35T cells indicated that there was more labile iron content in F35T cells in comparison to B4G12 cells as both cell types were protected with the same dose of DFO of 100 μM. These findings indicate that F35T cells were less protected by DFO because

of comparatively higher cytosolic iron content, leading them to be more prone to ferroptosis than healthy cells.

We also probed FECD disease and healthy cultured cell models to determine alterations to key genes and proteins known to occur in ferroptosis. In our study, F35T cells had 2.27-fold higher *GPX4* gene expression when compared with HCEC-B4G12 cells ($p < 0.01$; **Fig. 2K**); however, F35T cells were found to have 53% lower GPX4 protein expression when compared to control B4G12 cells in western blot analysis **(**$p < 0.001$; **Fig. 2K)**. F35T cells showed significantly higher *SOD2* gene expression by 3.37-fold when compared with HCEC-B4G12 cells ($p < 0.01$; **Fig. 2L**). There was no significant difference in SOD2 protein expression in between these two cell lines ($p = 0.71$; **Fig. 2L**). *NRF2* gene expression was also found to be upregulated by 3.03-fold in F35T cells when compared with HCEC-B4G12 cells ($p < 0.01$; **Fig. 2M**). There was no significant difference in NRF2 protein expression was observed in these cell line ($p = 0.10$; **Fig. 2M**). *FSP1* gene expression was increased by 2.52-fold in F35T cells when compared with B4G12 cells **(**$p < 0.01$; **Fig. 2N)**. FSP1 protein expression was also increased by 38% in F35T cells when compared with control B4G12 cells in western blot analysis **(**$p < 0.001$; **Fig. 2N)**. Of note, FSP1 expression in cells strongly correlated with the expression found in FECD tissues. F35T cells had upregulation of *FPN1* gene expression by 4.3-fold when compared with HCEC-B4G12 cells ($p < 0.001$; **Fig. 2O)**. F35T cells also had upregulation of ACSL4 gene expression by 1.88-fold in comparison to B4G12 cells ($p < 0.01$; **Fig. 2P)**. Overall, *GPX4*, *SOD2*, *NRF2*, *FP1* and *ACSL4* genes were upregulated in FECD cell culture whereas in FECD tissues, these genes were downregulated except FSP1 was upregulated in both FECD cell culture and tissues. FECD cell culture model showed upregulation of NRF2 and FSP1 protein like FECD tissues. However, SOD protein expression was downregulated in FECD tissues but upregulated in FECD cells.

TFR1 expression correlates with increased lipid peroxidation, iron accumulation, and loss of GPX4 activity and is a useful biomarker of ferroptosis in FECD patient samples and cell cultures.

Transferrin receptor (TFR1), which internalizes transferrin-iron complexes through endocytosis, has been identified as the most specific ferroptosis marker because this receptor is required for importing iron (33). TFR1 protein has been found to be upregulated in cells undergoing ferroptosis, and thus TFR1 upregulation serves as a useful marker of ferroptosis because it contributes to higher iron intake and correlates with iron-mediated lipid peroxidation (33). Therefore, we tested for levels of TFR1 gene and protein expression in human surgical samples from patients with FECD compared to healthy donor tissue samples. Although *TFR1* gene expression was significantly downregulated in FECD tissues ($p < 0.05$; **Fig. 3A**), TFR1 protein expression was found to be 47% higher in FECD tissues when compared with healthy control tissues ($p < 0.01$, **Fig. 3A**). TFR1 gene and protein expression were also quantified in both diseased F35T and healthy HCEC-B4G12 cell culture models. In contrast to FECD tissue samples, F35T cells had upregulation of *TFR1* gene expression by 4.77-fold compared to HCEC-B4G12 cells ($p < 0.01$, **Fig. 3B**). In concert with FECD tissue samples, we found significant upregulation of TFR1 protein expression by 5.40-fold when compared with B4G12 cells ($p < 0.001$, **Fig. 3B**). Upregulation of both TFR1 protein and mRNA indicated that FECD cells are more prone to excessive uptake iron and ferroptotic cell damage.

To quantify mitochondrial superoxide in FECD cells and controls, F35T and HCEC-B4G12 cell cultures were exposed to MitoROS 580 dye. As a positive control both cell types were also exposed to 50 μM AMA. F35T cells showed 15.7-fold higher basal mitochondrial superoxide concentrations ($p < 0.0001$, **Fig. 3C**) than healthy control cells. Basal levels of ROS were also quantified by dihydroethidium (DHE) fluorescent probe. Flow cytometry analyses showed

3.29-fold higher ROS in F35T cells when compared with HCEC-B4G12 cells ($p < 0.0001$, **Fig. 3D**). Confocal microscopy images also showed greater DHE fluorescence in F35T cells (**Fig. 3E**).

Ferroptosis has been reported to be closely associated with lipid metabolism and lipid storage in droplets (82-84). Degradation of intracellular lipid droplets promote ferroptosis and it has been reported that accumulation of lipid droplets increases during early stage of ferroptosis but decreases at the late stage of ferroptosis (82). Lipid droplet concentrations were quantified by flow cytometry using a LipidSpot™ 610 fluorescent probe. Flow cytometry analysis showed 2.29-fold higher amount of lipid droplets in F35T cells in comparison to HCEC-B4G12 cells ($p < 0.0001$, **Fig. 3F**). Confocal microscopy images showed a higher number of lipid droplets in F35T cells (**Fig. 3G**).

Iron overload in FECD is mediated by decreased ferritin and increased transferrin.

Ferritin is a common protein readily available in all cells, and its main function is to form structures that can store cellular iron and prevent iron-mediated toxicity and oxidative stress (85). Cells get an influx of ferric iron (Fe^{3+}) as transferrin-bound iron through transferrin receptor 1 (TFRC)-mediated endocytosis; Fe^{3+} then gets reduced to ferrous iron (Fe^{2+}) in the endosome by STEAP3 and released to the cytoplasm via SLC11A2 (**Fig. 4A**) (86). Ferritin can store labile Fe^{2+} inside its multimeric shell in a nontoxic state and releases it as required depending on the consumption of iron during oxygen transport, Fe-S production in the mitochondria, and efflux transport via ferroportin (86). In addition to the iron overload due to higher iron uptake associated with TFR1 overexpression, downregulation of ferritin protein via ferritinophagy or other cellular processes can lead to accumulation of toxic Fe^{2+} and result in increased susceptibility to ferroptosis (86). Since ferritin plays a crucial role in iron

homeostasis, we quantified human ferritin in protein extracted from both F35T and HCEC-B4G12 cell types using the Human Ferritin ELISA kit. Healthy HCEC-B4G12 cells had 28.63±1.01 ng of ferritin/mg of protein whereas F35T cells had 23.88±0.45 ng/mg of protein (**Fig. 4B**). F35T cells had significantly ($p < 0.001$) lower ferritin/mg of protein than in B4G12 cells. These findings demonstrate that F35T cells have less cytosolic ferritin in the FECD disease state than encountered in healthy cells, and indicates that hindered iron storage in FECD pathobiology associated with increased labile Fe^{2+} iron inside diseased cells may result in greater susceptibility to ferroptosis.

Mitochondrial ferritin (FtMt) protein is structurally and functionally analogous to cytosolic human ferritin and plays a crucial role in cellular iron homeostasis via the storage of toxic labile iron within mitochondria (87). Previously, it has been found that overexpression of FtMt in mitochondria can cause the redistribution of iron from the cytosol to mitochondria, resulting in a decrease of the cytosolic iron accumulation (88, 89). FtMt has also been reported to play a major role in protecting mitochondria from iron-mediated oxidative damage in addition to its iron storage function (90, 91). Therefore, we quantified FtMt in protein extracted from both cell types using the Mitochondrial Ferritin ELISA kit. Healthy HCEC-B4G12 cells were found to have 175.16±3.94 ng of MtFt/mg of protein whereas F35T cells had 101.72±3.87 ng/mg of protein (**Fig. 4C**). F35T cells had 1.72-fold lower FtMt/mg of protein than in HCEC-B4G12 cells ($p < 0.0001$). These findings indicated that F35T cells had very low FtMt compared to healthy cells, potentially hampering iron redistribution from cytosol to mitochondria as well as mitochondrial iron storage and leading to toxic iron accumulation and iron-mediated oxidative damage. Lower than normal FtMt can disrupt cellular iron metabolism and increase cellular ROS levels dramatically (87).

Ferritin in humans consists of both heavy and light chains encoded by the FTH and FTL genes, respectively (92). FECD surgical tissue samples showed downregulation of both FTH and FTL mRNA by 0.24 and 0.36-fold, respectively, in comparison to healthy control tissues ($p < 0.0001$, **Fig. 4D** and $p < 0.01$, **Fig. 4E**, respectively**)**. In contrast, F35T cells cultures showed upregulation of both FTH and FTL mRNA by 2.37 and 2.64-fold, respectively, in comparison to control tissues ($p < 0.05$, **Fig. 4F** and $p < 0.05$, **Fig. 4G**, respectively**)**. These perturbations may reflect changes attributable to disease stage and/or model differences.

A total of 23,171 protein isoforms were identified (**STable 1**), of which 3,448 protein isoforms had significantly altered expression in FECD patient aqueous compared to non-FECD aqueous samples (**STable 2**). A molecular pathway analysis of the statistically significant proteins ($p < 0.05$) between FECD and control aqueous humor samples collected from patients undergoing endothelial keratoplasty identified several groups of functionally related proteins. The top 15 most significantly represented pathways determined by IPA software (Qiagen) included ferroptosis. Of greatest relevance to this study was the statistically significant difference in transferrin protein in the aqueous humor. Several isoforms of human transferrin (UniProtKB IDs: F8WEK9, F8WCI6, P02787, A0PJA6, F8WC57, B4DHZ6, C9JVG0, Q06AH7, AND C9JB55) were higher in FECD aqueous samples compared to controls ($3.8 < \text{Ratio} < 18.7$; $p < 0.015$). A complete list of differentially expressed proteins by molecular pathway can be found in **STable 3**, including the complete list of ferroptosis proteins significantly different in aqueous samples of FECD patients compared to controls. Findings indicate that transferrin levels in aqueous may be a potential biomarker and indicator of ferroptosis activity in FECD.

FECD mutation is associated with cytosolic and mitochondrial iron accumulation after UVA exposure.

UVA a major component of prolonged sunlight exposure that can cause severe oxidative stress in exposed cells (93, 94). It has been well reported that UVA irradiation of cells increases labile cytosolic Fe^{2+} release from the core of cytosolic and mitochondrial ferritin through the ferritin degradation process, leading to the accumulation of potentially harmful iron forms (42, 44, 94). Herein, we exposed human donor corneas to UVA irradiation of 5 J/cm^2, and cytosolic Fe^{2+} content was detected in isolated primary endothelial cells using FerroOrange fluorescent probe via flow cytometry. Dose screening using MTS assay showed that UVA irradiation of 5 J/cm^2 is a relatively safe physiological dose (**Fig. *S3***). Upon UVA irradiation, labile cytosolic Fe^{2+} was markedly increased in pair-wise comparison with control unexposed corneas ($p = 0.28$; **Fig. 4H, 4I**). These findings indicated that the human cornea is susceptible to UVA irradiation mediated labile iron release and accumulation in the cytosolic compartment.

Next, we exposed both F35T and HCEC-B4G12 cells to various doses of UVA irradiation of 1, 2, 4 and 8 J/cm^2. Upon irradiation, both cytosolic and mitochondrial Fe^{2+} were quantified and compared by measuring fluorescence using a flow cytometry. When HCEC-B4G12 cells were irradiated with UVA, there was maximum 8.1% increase of cytosolic Fe^{2+} at the dose of 4 J/cm^2, whereas F35T cells had a massive 60.01% increase at the same dose level (**Fig. 4J**). F35T cells had significantly ($p < 0.0001$) higher percentage of Fe^{2+} release from ferritin when compared with healthy B4G12 cells at all doses of UVA irradiation, which indicated that F35T cells are more susceptible to UVA irradiation mediated toxic iron release and accumulation. At higher dose of 8 J/cm^2, we observed a decrease of percent increase of cytosolic iron in comparison to the dose of 4 J/cm^2. In our UVA dose screening, we observed that dose above 5 J/cm^2 is toxic to F35T cells (**Fig. *S3***); therefore, potential cell death might be associated with this finding. We also studied mitochondrial iron release with UVA irradiation. HCEC-B4G12 cells had maximum of 9.84% iron release at the dose of 1 J/cm^2, whereas F35T cells had a

28.52% increase of mitochondrial iron at the same low dose (**Fig. 4K**). F35T cells had significantly higher percentage of mitochondrial iron release when compared with HCEC-B4G12 cells at all doses of UVA irradiation ($p < 0.0001$, **Fig. 4K**). Therefore, F35T cells were significantly and dramatically more susceptible to UVA irradiation mediated mitochondrial iron release, which can lead to iron accumulation and iron-mediated oxidative damage of mitochondria. At higher dose levels of 4 and 8 J/cm^2, we observed dramatic decreases in mitochondrial iron. It has been reported that higher UVA irradiation (e.g. >100 mJ/cm^2) causes mitochondrial fragmentation (95, 96). Mitochondrial fragmentation can potentially cause the release of mitochondrial iron into the cytosol, and thereby affect the quantification of true mitochondrial iron by reducing the sensitivity of the mitochondria selective fluorescence probe used quantify mitochondrial iron. Considering the physiological daily UVA irradiation that corneas receive from sunlight exposure, our data suggest that chronic Fe^{2+} release may form the mechanistic basis for UVA mediated oxidative damage that contributes to FECD disease progression.

Pretreatment with solubilized ubiquinol prevents lipid peroxidation and cell death after direct RSL3 ferroptosis induction in FECD and healthy cell cultures.

RSL3, a potent ferroptosis inducer, was used to induce lipid peroxidation in both HCEC-B4G12 and F35T cells. RSL3 directly inhibits GPX4, thereby lowering the antioxidant capacity of cells and increasing levels of lipid peroxides leading to cell death by ferroptosis (**Fig. 5A**) (32, 80). Ubiquinol is an endogenous antioxidant that is converted from coenzyme Q10 via ferroptosis suppressor protein 1 (FSP1) and provides some degree of protection against ferroptosis and lipid peroxidation (97). Previously, we developed a highly dispersible solubilized ubiquinol that showed significant protection against lipid peroxidation and ferroptosis in a dose-dependent manner in donor corneal endothelial cells (30). Herein, we

treated both cell types with solubilized ubiquinol at different concentrations of 1, 10, 50, and 100 μM to examine its efficacy in preventing lipid peroxidation in a dose-dependent manner. We found that RSL3 at a 1 μM dose induced lipid peroxidation in untreated cells as indicated by the peak shift of the BODIPY fluorescent probe from red to green. Solubilized ubiquinol treatment at all the tested concentrations significantly inhibited lipid peroxidation in both cell types when compared to cells treated with RSL3 alone ($p < 0.0001$; **Fig. 5B, 5C**). Solubilized ubiquinol showed a clear dose-dependent inhibition pattern from 1 to 5 μM doses in HCEC-B4G12 cells while in F35T cells, dose-dependent inhibition was detected until the 10 μM dose but higher doses did not confer more protection. Dose-dependent inhibition at higher doses also was not observed in HCEC-B4G12 cells; at the 1 μM dose, solubilized ubiquinol completely inhibited lipid peroxidation to a degree that was equal to basal levels in both the no-RSL3 and no-treatment groups. Lipid peroxidation inhibition with soluble ubiquinol reached basal levels at the 10 μM dose in F35T cells; however, the basal lipid peroxidation levels were significantly higher in F35T cells than HCEC-B4G12 cells ($p < 0.0001$). Solubilized ubiquinol treatment at the same doses was more effective in inhibiting lipid peroxidation in HCEC-B4G12 cells than F35T cells, which indicates a higher susceptibility of F35T cells to ferroptosis and lipid peroxidation. At the 1 μM dose, solubilized ubiquinol inhibited lipid peroxidation by 43.08% compared to the RSL3 only group in HCEC-B4G12 cells, whereas only 12.45% inhibition was observed in F35T cells. Similarly, at a 10 μM dose, 62.35% inhibition was noticed in B4G12 cells while 49.24% inhibition happened in F35T cells (**Fig. 5C, 5D**). These findings indicate that F35T cells were more susceptible to lipid peroxidation and ferroptosis, and solubilized ubiquinol was highly effective in inhibiting detrimental cellular processes and protecting corneal endothelial cell health.

We also assessed F35T and HCEC-B4G12 cell viability with and without solubilized ubiquinol following treatment with RSL3 using a LDH assay. A ferroptosis inhibitor, ferrostatin-1, was used as a positive control to validate that cell death was caused by the ferroptosis process. Solubilized ubiquinol significantly inhibited RSL3 induced ferroptosis event at a very low dose of 1 μM in both cell types (**Fig. 6A**). RSL3 caused significantly more cell death in F35T cells compared to HCEC-B4G12 cells, which indicated their higher susceptibility to ferroptosis and aligned with the findings of higher basal lipid peroxidation in F35T cells (**Fig. 6B**). Light microscopy images showed no morphological damage when cells were treated with solubilized ubiquinol even at the low concentration of 1 μM (**Fig. 6C**). Solubilized ubiquinol treatment at all concentrations tested underperformed in F35T cells compared to HCEC-B4G12 cells, which indicated higher susceptibility of F35T cells to ferroptosis. However, solubilized ubiquinol at higher concentrations from 5 to 100 μM increased cell numbers indicating possible F35T cell proliferation in addition to protecting F35T cells from ferroptosis.

When cells were challenged with RSL3, we observed a dramatic increase of lipid droplets in both cell lines, and F35T cells showed notably more droplets when compared with HCEC-B4G12 cells (**Fig. 6D**). In live time-lapse video analysis, we observed that the number of lipid droplets decreased dramatically during ferroptosis mediated cell death; almost no droplets were visible in the periphery, and droplets condensed closer to the nucleus (**Fig. 6E, Supplementary video 1A, 1B**). We also observed that F35T cells died 1 h earlier than B4G12 cells when treated with same dose of RSL3 (**Fig. 6E, Supplementary video 1A, 1B, 2A, 2B**). F35T cells also demonstrated a wave-like spreading pattern of ferroptotic lipid damage as reported in the literature (98). We observed a portion of the cell population to be completely dead as indicated by SYTOX green while another portion to be alive in the same well in the tissue culture dish **(Fig. *S4*)**.

Solubilized ubiquinol performed better than antioxidant N-acetyl cysteine (NAC) and ferroptosis inhibitor deferoxamine (DFO). In the MTS-based RSL3 induced ferroptosis assay, solubilized ubiquinol at the concentrations of 1 and 10 μM showed significantly higher cell viability in comparison to N-acetyl cysteine (NAC) and deferoxamine (DFO) at the same concentrations (**Fig. 6F**). Solubilized ubiquinol also outperformed another potent antioxidant and known ferroptosis inhibitor, ferrostatin-1, at the 1μM dose. These findings indicated that solubilized ubiquinol may be better suited to counter ferroptosis in FECD than the other agents tested in this series.

DISCUSSION

While the genetic background of FECD is complex and age of onset varies based on genotype, the clinically recognized hallmarks of this disease are highly conserved. CTG trinucleotide repeat expansions in intron 3 of the *TCF4* gene are found in more than 70% of patients with FECD; patients with this genotypic marker tend to develop "late-onset" disease and tend to be female (3- to 4:1 ratio). Although the exact mechanism of disease remains incompletely understood, it is possible that expressed non-coding regions of mRNA are toxic to CECs. The remaining portion of patients have a mutation in one of at least 10 known genes with a disease-causing mutation that affect a variety of CEC functions, from abnormal collagen production to altered ion channel pump function. Remarkably, all forms of this disease are characterized by an increased susceptibility to oxidative stress, regardless of genotype, age of onset, or gender. Our analysis of surgical samples collected at the time of endothelial keratoplasty for patients with FECD that were pooled and performed on ungenotyped patients. This broad approach bears direct correlation with the FECD clinical phenotypes common to end-stage disease (loss of CECs, confluent guttae on the inner cornea, corneal edema and vision loss). It is noteworthy

that we found evidence of lipid peroxidation, cytosolic Fe^{2+} accumulation, and GPX4 depletion occurring in tandem in surgical samples. Our findings, which are contextualized by the well-documented background of ROS accumulation, support the general presence of increased susceptibility to ferroptosis in patients with FECD. Although we include additional cell culture evidence that the *TCF4* trinucleotide repeat expansion increases ferroptosis susceptibility, further studies are needed to determine if these findings apply to other FECD genotypes equally.

Previously, we showed that ferroptosis can be induced experimentally in healthy immortalized human CECs using erastin, a direct inhibitor of system x_c^- and the GSH synthetic pathway. In this study, we found evidence that FECD is associated with constitutive increases in cytosolic Fe^{2+} and lipid peroxidation as well as decreased GPX4, specifically in primary and immortalized *in vitro* patient-derived FECD cell culture models harboring CTG repeat expansions in *TCF4*. Multiple lines of evidence support the theoretical basis for ferroptosis to be a pathological component of cell death in FECD. Nrf2, the stress-induced transcription factor that serves as the master regulator of endogenous antioxidant response element, becomes upregulated in response to a variety of endogenous and exogenous stressors (64, 99, 100). Nrf2 has also been shown to regulate the activity of several ferroptosis and lipid peroxidation-related proteins involved in both iron and GSH metabolism, including SLC7A11 which encodes the cystine/glutamate antiporter (system x_c^-) that increases resistance to ferroptosis (101-104). In FECD, Nrf2 protein levels have been found to be decreased (12). The main regulator of Nrf2, DJ-1, is also downregulated in FECD, which can also lead to increased susceptibility of CECs to UVA induced damage (25). In addition to decreases in Nrf2, redox sensor peroxiredoxin 1 (PRDX1) downregulation in FECD makes CECs more sensitive to cell death associated with lipid peroxidation because both Nrf2 and PRDX1 are required to regulate lipid peroxidation

(4). These reports indicate strong evidence for higher susceptibility to lipid peroxidation and ferroptosis in FECD. The *TCF4* genotype models utilized in this study reproduce the ferroptosis pathway signatures found in both diseased tissue and direct experimental induction in healthy cells. Our findings are a strong indication that intronic repeat expansions likely render the FECD endothelium more susceptible to ferroptosis, and underscore the utility of these models – both primary and immortalized FECD cell lines, which returned similar data – in further studies of ferroptosis in FECD. They also suggest possible directions for investigating ferroptosis in other trinucleotide repeat expansions diseases, such as Huntington's.

In this study elevated levels of Fe^{2+}, a reactive redox substrate under strict control and regulation, were detected in the cytosol of corneal endothelial cells from FECD patient samples and all cell culture models tested. While the notion that iron overload plays a part in the pathobiology of Fuchs dystrophy is novel, it is well known that dysregulation of iron metabolism plays a role in several diseases. Typically, iron enters the cell from surrounding fluid after complexation with transferrin, a secretory product that binds Fe^{3+} (**Fig. 7**). The transferrin-Fe^{3+} complex enters via TFR1-mediated endocytosis, becomes acidified and reduced to Fe^{2+} in endosomes by STEAP3 metalloreductase, and gets released into the cytosol where it is converted to Fe^{3+} and incorporated into ferritin, a key iron storage protein and major regulator of intracellular iron (61, 72). Cells normally maintain low free cytosolic Fe^{2+} levels in a steady-state equilibrium with ferritin-bound iron because free Fe^{2+} is highly reactive and potentially toxic. Fe^{2+} can generate excessive ROS via Fenton reactions and increase the activity of lipoxygenases that are responsible for lipid peroxidation (72, 94). Thus, our finding of cytosolic Fe^{2+} accumulation in patient and cell culture models is noteworthy because it implicates ferroptosis as a mechanism of oxidative cell death in FECD. In ferroptosis, the

sequence of Fe^{2+}-mediated plasma membrane lipid peroxidation and subsequent cell death results in affected cells adopting a characteristic morphological appearance that features redistribution of lipids at the PM, occurring as lipid blebbing and bubble formation and leading toward cellular ballooning prior to death. Although we were unable to visualize ferroptosis cell morphology sequences in tissue explants owing to their terminal degeneration at the end stage of disease, we were able to visualize plasma membrane lipid degeneration and migration of pooled lipids toward the nuclear envelope in cultured FECD cells, confirming ferroptosis cell death sequences of affected cells.

We detected several points of disruption in iron regulation attributable to FECD genotype, including increased iron uptake signaling and storage disequilibrium. First, cultured FECD CECs with *TCF4* repeat expansions show increased levels of ferroportin, the only membrane bound protein responsible for iron efflux. Regulated by Nrf2 signaling under states of oxidative stress, an increase in ferroportin expression indicates the cellular attempt to remove excess iron from the cytosol. *FPN1* expression has been reported be regulated by Hif1α, Hif2α and the Hif response element (HRE) under anemic conditions, which would cause increase to get more iron into the blood from cells, and is regulated by Nrf2 in response to oxidative stress (105). *FPN1* transcription is also regulated by Nrf2 in response to inflammation and in FECD there is evidence of inflammation (106). In addition, increased amounts of transferrin, the secreted iron carrier protein necessary for uptake by cells, were detected in aqueous samples from patients with FECD at the time of transplant surgery. Increased transcription and expression of TFR1, the membrane bound receptor that endocytoses ferritin-Fe^{3+} complexes, was also detected in surgical tissue samples and all cell culture models. As well, decreased levels of cytosolic ferritin were found in cell culture models. The cell behavior observed with respect to iron uptake and storage is consistent with iron scavenging and decreased storage capacity, and

these findings may direct future investigations into iron storage regulation and ferritin recycling via ferritinophagy. Interestingly, we also found a corresponding decrease in levels of mitochondrial ferritin, which like its cytosolic counterpart regulates mitochondrial iron and indicates the potential for Fe^{2+} overload in disease-affected CEC mitochondria. Mitochondrial impairment in FECD has been described rather extensively, with findings that include increased membrane depolarization, decreased ATP synthesis, decreased mtDNA, and increased mitophagy. In this study we did not measure mitochondrial iron levels, mitochondrial membrane lipid peroxidation, or other indicators of ferroptosis in FECD mitochondria. However, mitochondria may be particularly resistant to ferroptosis due to the presence of a third independent antioxidant defense enzyme, dihydroorotate dehydrogenase (DHODH), that is located on the outer face of the mitochondrial inner membrane and, like FSP1, directly supports the biosynthetic recycling of ubiquinol.

We found further evidence of the centrality of Fe^{2+} and importance of lipid peroxidation in FECD disease progression through UVA irradiation and ferroptosis suppression experiments. We first found that increased sensitivity to UV-induced oxidative damage in *TCF4* FECD cell culture models was mediated by Fe^{2+} accumulation. After treating cultured cells with physiologic levels of UVA, we detected increased cytosolic levels of Fe^{2+} in FECD cells compared to controls treated with the same exposures; this response was dose dependent. UVA is a well-known risk factor for FECD disease progression, yet the mechanism by which UV causes oxidative damage in FECD has not been characterized previously. UVA is known to increase cytosolic Fe^{2+} by causing release from ferritin (41, 42, 107). In skin, UVA causes lipid peroxidation in cell membranes via pathways involving Fe (94, 108, 109); ferritin degradation within hours that results in immediate Fe^{2+} increases (107); and compensatory increases in ferritin days after exposure (107, 110). Our findings support current understandings of the role

of ultraviolet as an accelerant of cell damage in FECD, and demonstrate the involvement of Fe^{2+} in the mechanism of disease progression. We next found that iron chelation with DFO conferred some protection against ferroptosis induced by the direct inhibition of GPX4 using RSL3. When RSL3 inhibits glutathione peroxidase 4 (GPX4), the labile iron pool causes lipid peroxidation and increases the accumulation of lipid ROS, resulting ferroptosis mediated cell death (80, 81). Therefore, a larger quantity of labile will increase the risk of ferroptosis when GPX4 is blocked by RSL3. F35T cells had significantly more cell death in comparison to HCEC-B4G12 cells at the same dose of RSL3 challenge and pre-treatment with DFO. DFO was less effective in preventing ferroptosis in F35T cells when compared with HCEC-B4G12 cells due to a comparatively higher labile iron pool. Therefore, this experiment simultaneously confirmed the presence of increased basal intracellular iron concentrations and susceptibility to cell death in immortalized FECD cells, and provided confirmatory evidence that iron is involved in FECD-associated cell death.

We also found that ferroptosis suppression is possible in FECD cell cultures by co-treatment with ubiquinol. Ubiquinol, the reduced and active form of coenzyme Q10, is an essential participant in the FSP1-CoQ10-NAD(P)H pathway, an independent system working in parallel with GPX4 and glutathione to suppress lipid peroxidation and ferroptosis by supporting FSP1 function (33, 111). This experiment demonstrated the ability to prevent cell death after direct induction of ferroptosis using RSL3 in immortalized FECD cells using a previously validated formulation of ubiquinol complexed with γ-cyclodextrin that increases ubiquinol availability to CECs by increasing drug bioavailability in the aqueous phase. By demonstrating that specific anti-ferroptosis agents can mitigate the iron-mediated lipid peroxidation present in cells with this common FECD genetic background, we simultaneously confirm the importance of ferroptosis as a mechanism by which characteristic phenotypic damage occurs in corneal

endothelial cells and establish the basis for investigating therapeutics to prevent ferroptosis-mediated damage and disease progression in FECD.

CONCLUSION

Overall, this investigation presents first-line evidence that ferroptosis is a mechanism by which oxidative damage and corneal endothelial cell death occur in Fuchs endothelial corneal dystrophy. We present evidence that expanded trinucleotide repeats in intron 3 of *TCF4* comprise a genetic background that results in increased cytosolic Fe^{2+}, iron-mediated lipid peroxidation, and increased susceptibility to ferroptosis. We also present evidence that UVA exposure in cells with expanded repeats in *TCF4* increases the risk of cell death via an iron-mediated mechanism, and highlight the importance of cytosolic Fe^{2+} accumulations as a plausible molecular mechanism for FECD disease progression. Experimental evidence demonstrating that both iron chelation and anti-ferroptosis antioxidant treatments prevent cell death in FECD cell cultures demonstrate the importance of these mechanisms. Although the evidence is strongest in this series for increased ferroptosis susceptibility in this *TCF4* genotype, our findings apply to other FECD genotypes and further studies are needed to explore this possibility.

Declaration of competing interest

The authors declare that the study was carried out without any known competing financial or commercial interests that could have influenced the findings described in this paper.

Acknowledgements

The authors cordially thank the Lyle and Sharon Bighley Endowed Chair of Pharmaceutical Sciences, Iowa Lions Eye Bank, the Beulah and Florence Usher Endowed Chair in

Cornea/External Disease and Refractive Surgery, the M.D. Wagoner & M.A. Greiner Cornea Excellence Fund, Mr. and Mrs. Robert and Joell Brightfelt, Mr. and Mrs. Lloyd and Betty Schermer, the UIHC Cornea Research Fund for financial support, and the cornea patients, donors, and donor families that made this research possible.

REFERENCES

1.Ołdak M, Ruszkowska E, Udziela M, Oziębło D, Bińczyk E, Ścieżyńska A, et al. Fuchs Endothelial Corneal Dystrophy: Strong Association with rs613872 Not Paralleled by Changes in Corneal Endothelial TCF4 mRNA Level. Biomed Res Int. 2015;2015:640234-.
2.Uchida T, Sakai O, Imai H, Ueta T. Role of Glutathione Peroxidase 4 in Corneal Endothelial Cells. Current Eye Research. 2017;42(3):380-5.
3.Lovatt M, Adnan K, Peh GSL, Mehta JS. Regulation of Oxidative Stress in Corneal Endothelial Cells by Prdx6. Antioxidants (Basel, Switzerland). 2018;7(12).
4.Lovatt M, Adnan K, Kocaba V, Dirisamer M, Peh GSL, Mehta JS. Peroxiredoxin-1 regulates lipid peroxidation in corneal endothelial cells. Redox biology. 2020;30:101417-.
5.America. EBAo. 2019 Eye Banking Statistical Report Web site. 2020 [
6.Wagoner MD, Bohrer LR, Aldrich BT, Greiner MA, Mullins RF, Worthington KS, et al. Feeder-free differentiation of cells exhibiting characteristics of corneal endothelium from human induced pluripotent stem cells. Biology open. 2018;7(5).
7.Joyce NC. Proliferative capacity of corneal endothelial cells. Experimental eye research. 2012;95(1):16-23.
8.Jalimarada SS, Ogando DG, Bonanno JA. Loss of ion transporters and increased unfolded protein response in Fuchs' dystrophy. Mol Vis. 2014;20:1668-79.
9.Liu C, Miyajima T, Melangath G, Miyai T, Vasanth S, Deshpande N, et al. Ultraviolet A light induces DNA damage and estrogen-DNA adducts in Fuchs endothelial corneal dystrophy causing females to be more affected. Proc Natl Acad Sci U S A. 2020;117(1):573-83.
10.Liu C, Vojnovic D, Kochevar IE, Jurkunas UV. UV-A Irradiation Activates Nrf2-Regulated Antioxidant Defense and Induces p53/Caspase3-Dependent Apoptosis in Corneal Endothelial Cells. Invest Ophthalmol Vis Sci. 2016;57(4):2319-27.
11.White TL, Deshpande N, Kumar V, Gauthier AG, Jurkunas UV. Cell cycle re-entry and arrest in G2/M phase induces senescence and fibrosis in Fuchs Endothelial Corneal Dystrophy. Free radical biology & medicine. 2021;164:34-43.
12.Jurkunas UV, Bitar MS, Funaki T, Azizi B. Evidence of oxidative stress in the pathogenesis of fuchs endothelial corneal dystrophy. Am J Pathol. 2010;177(5):2278-89.
13.Zinflou C, Rochette PJ. Ultraviolet A-induced oxidation in cornea: Characterization of the early oxidation-related events. Free radical biology & medicine. 2017;108:118-28.
14.Delic NC, Lyons JG, Di Girolamo N, Halliday GM. Damaging Effects of Ultraviolet Radiation on the Cornea. Photochemistry and photobiology. 2017;93(4):920-9.
15.Czarny P, Kasprzak E, Wielgorski M, Udziela M, Markiewicz B, Blasiak J, et al. DNA damage and repair in Fuchs endothelial corneal dystrophy. Molecular biology reports. 2013;40(4):2977-83.
16.Halilovic A, Schmedt T, Benischke AS, Hamill C, Chen Y, Santos JH, et al. Menadione-Induced DNA Damage Leads to Mitochondrial Dysfunction and Fragmentation During Rosette Formation in Fuchs Endothelial Corneal Dystrophy. Antioxidants & redox signaling. 2016;24(18):1072-83.
17.Kumar V, Jurkunas UV. Mitochondrial Dysfunction and Mitophagy in Fuchs Endothelial Corneal Dystrophy. Cells. 2021;10(8).
18.Moysan A, Marquis I, Gaboriau F, Santus R, Dubertret L, Morlière P. Ultraviolet A-induced lipid peroxidation and antioxidant defense systems in cultured human skin fibroblasts. The Journal of investigative dermatology. 1993;100(5):692-8.
19.Vats K, Kruglov O, Mizes A, Samovich SN, Amoscato AA, Tyurin VA, et al. Keratinocyte death by ferroptosis initiates skin inflammation after UVB exposure. Redox Biology. 2021;47:102143.

20.Jurkunas UV, Bitar MS, Funaki T, Azizi B. Evidence of oxidative stress in the pathogenesis of fuchs endothelial corneal dystrophy. The American journal of pathology. 2010;177(5):2278-89.
21.Jurkunas UV, Rawe I, Bitar MS, Zhu C, Harris DL, Colby K, et al. Decreased expression of peroxiredoxins in Fuchs' endothelial dystrophy. Investigative ophthalmology & visual science. 2008;49(7):2956-63.
22.Gottsch JD, Bowers AL, Margulies EH, Seitzman GD, Kim SW, Saha S, et al. Serial analysis of gene expression in the corneal endothelium of Fuchs' dystrophy. Invest Ophthalmol Vis Sci. 2003;44(2):594-9.
23.Buddi R, Lin B, Atilano SR, Zorapapel NC, Kenney MC, Brown DJ. Evidence of oxidative stress in human corneal diseases. The journal of histochemistry and cytochemistry : official journal of the Histochemistry Society. 2002;50(3):341-51.
24.Lovatt M, Kocaba V, Hui Neo DJ, Soh YQ, Mehta JS. Nrf2: A unifying transcription factor in the pathogenesis of Fuchs' endothelial corneal dystrophy. Redox Biology. 2020;37:101763.
25.Liu C, Chen Y, Kochevar IE, Jurkunas UV. Decreased DJ-1 leads to impaired Nrf2-regulated antioxidant defense and increased UV-A-induced apoptosis in corneal endothelial cells. Invest Ophthalmol Vis Sci. 2014;55(9):5551-60.
26.Yang Wan S, SriRamaratnam R, Welsch Matthew E, Shimada K, Skouta R, Viswanathan Vasanthi S, et al. Regulation of Ferroptotic Cancer Cell Death by GPX4. Cell. 2014;156(1):317-31.
27.Forcina GC, Dixon SJ. GPX4 at the Crossroads of Lipid Homeostasis and Ferroptosis. Proteomics. 2019;19(18):e1800311.
28.Nikitina AS, Belodedova AV, Malyugin BE, Sharova EI, Kostryukova ES, Larin AK, et al. Dataset on transcriptome profiling of corneal endothelium from patients with Fuchs endothelial corneal dystrophy. Data Brief. 2019;25:104047-.
29.Wieben ED, Aleff RA, Tang X, Kalari KR, Maguire LJ, Patel SV, et al. Gene expression in the corneal endothelium of Fuchs endothelial corneal dystrophy patients with and without expansion of a trinucleotide repeat in TCF4. PloS one. 2018;13(7):e0200005.
30.Naguib YW, Saha S, Skeie JM, Acri T, Ebeid K, Abdel-rahman S, et al. Solubilized ubiquinol for preserving corneal function. Biomaterials. 2021;275:120842.
31.Dixon SJ, Lemberg KM, Lamprecht MR, Skouta R, Zaitsev EM, Gleason CE, et al. Ferroptosis: an iron-dependent form of nonapoptotic cell death. Cell. 2012;149(5):1060-72.
32.Li J, Cao F, Yin H-l, Huang Z-j, Lin Z-t, Mao N, et al. Ferroptosis: past, present and future. Cell Death & Disease. 2020;11(2):88.
33.Feng H, Schorpp K, Jin J, Yozwiak CE, Hoffstrom BG, Decker AM, et al. Transferrin Receptor Is a Specific Ferroptosis Marker. Cell Reports. 2020;30(10):3411-23.e7.
34.Bogdan AR, Miyazawa M, Hashimoto K, Tsuji Y. Regulators of Iron Homeostasis: New Players in Metabolism, Cell Death, and Disease. Trends in Biochemical Sciences. 2016;41(3):274-86.
35.Venkataramani V. Iron Homeostasis and Metabolism: Two Sides of a Coin. Advances in experimental medicine and biology. 2021;1301:25-40.
36.Girotti AW. Lipid hydroperoxide generation, turnover, and effector action in biological systems. Journal of lipid research. 1998;39(8):1529-42.
37.Girotti AW, Kriska T. Role of lipid hydroperoxides in photo-oxidative stress signaling. Antioxidants & redox signaling. 2004;6(2):301-10.
38.Aust SD, Morehouse LA, Thomas CE. Role of metals in oxygen radical reactions. Journal of free radicals in biology & medicine. 1985;1(1):3-25.
39.Clemente SM, Martínez-Costa OH, Monsalve M, Samhan-Arias AK. Targeting Lipid Peroxidation for Cancer Treatment. Molecules (Basel, Switzerland). 2020;25(21).

40.Halliwell B, Gutteridge JM. Biologically relevant metal ion-dependent hydroxyl radical generation. An update. FEBS letters. 1992;307(1):108-12.
41.Aubailly M, Santus R, Salmon S. Ferrous ion release from ferritin by ultraviolet-A radiations. Photochemistry and photobiology. 1991;54(5):769-73.
42.Wolszczak M, Gajda J. Iron release from ferritin induced by light and ionizing radiation. Research on Chemical Intermediates. 2010;36(5):549-63.
43.Zhu J, Dai P, Liu F, Li Y, Qin Y, Yang Q, et al. Upconverting Nanocarriers Enable Triggered Microtubule Inhibition and Concurrent Ferroptosis Induction for Selective Treatment of Triple-Negative Breast Cancer. Nano letters. 2020;20(9):6235-45.
44.Smith MJ, Fowler M, Naftalin RJ, Siow RCM. UVA irradiation increases ferrous iron release from human skin fibroblast and endothelial cell ferritin: Consequences for cell senescence and aging. Free Radical Biology and Medicine. 2020;155:49-57.
45.Vile GF, Tyrrell RM. Oxidative stress resulting from ultraviolet A irradiation of human skin fibroblasts leads to a heme oxygenase-dependent increase in ferritin. Journal of Biological Chemistry. 1993;268(20):14678-81.
46.Afshari NA, Igo RP, Morris NJ, Stambolian D, Sharma S, Pulagam VL, et al. Genome-wide association study identifies three novel loci in Fuchs endothelial corneal dystrophy. Nature Communications. 2017;8(1):14898.
47.Wieben ED, Aleff RA, Rinkoski TA, Baratz KH, Basu S, Patel SV, et al. Comparison of TCF4 repeat expansion length in corneal endothelium and leukocytes of patients with Fuchs endothelial corneal dystrophy. PloS one. 2021;16(12):e0260837.
48.Fautsch MP, Wieben ED, Baratz KH, Bhattacharyya N, Sadan AN, Hafford-Tear NJ, et al. TCF4-mediated Fuchs endothelial corneal dystrophy: Insights into a common trinucleotide repeat-associated disease. Progress in retinal and eye research. 2021;81:100883.
49.Rinkoski TA, Bahler CK, Pacheco JM, Khanna ML, Holmes DM, Roy Chowdhury U, et al. Characterization of a dual media system for culturing primary normal and Fuchs endothelial corneal dystrophy (FECD) endothelial cells. PloS one. 2021;16(9):e0258006.
50.Zhu C, Joyce NC. Proliferative Response of Corneal Endothelial Cells from Young and Older Donors. Investigative Ophthalmology & Visual Science. 2004;45(6):1743-51.
51.Chu Y, Hu J, Liang H, Kanchwala M, Xing C, Beebe W, et al. Analyzing pre-symptomatic tissue to gain insights into the molecular and mechanistic origins of late-onset degenerative trinucleotide repeat disease. Nucleic acids research. 2020;48(12):6740-58.
52.Dobin A, Davis CA, Schlesinger F, Drenkow J, Zaleski C, Jha S, et al. STAR: ultrafast universal RNA-seq aligner. Bioinformatics (Oxford, England). 2013;29(1):15-21.
53.Robinson MD, McCarthy DJ, Smyth GK. edgeR: a Bioconductor package for differential expression analysis of digital gene expression data. Bioinformatics (Oxford, England). 2010;26(1):139-40.
54.Zhou N, Bao J. FerrDb: a manually curated resource for regulators and markers of ferroptosis and ferroptosis-disease associations. Database : the journal of biological databases and curation. 2020;2020.
55.Wisniewski JR, Zougman A, Nagaraj N, Mann M. Universal sample preparation method for proteome analysis. Nat Methods. 2009;6(5):359-62.
56.Rappsilber J, Mann M, Ishihama Y. Protocol for micro-purification, enrichment, pre-fractionation and storage of peptides for proteomics using StageTips. Nat Protoc. 2007;2(8):1896-906.
57.Chambers MC, Maclean B, Burke R, Amodei D, Ruderman DL, Neumann S, et al. A cross-platform toolkit for mass spectrometry and proteomics. Nat Biotechnol. 2012;30(10):918-20.
58.Sturm M, Bertsch A, Gropl C, Hildebrandt A, Hussong R, Lange E, et al. OpenMS - an open-source software framework for mass spectrometry. BMC Bioinformatics. 2008;9:163.

59.Craig R, Beavis RC. TANDEM: matching proteins with tandem mass spectra. Bioinformatics. 2004;20(9):1466-7.
60.Geer LY, Markey SP, Kowalak JA, Wagner L, Xu M, Maynard DM, et al. Open mass spectrometry search algorithm. J Proteome Res. 2004;3(5):958-64.
61.Xu C, Sun S, Johnson T, Qi R, Zhang S, Zhang J, et al. The glutathione peroxidase Gpx4 prevents lipid peroxidation and ferroptosis to sustain Treg cell activation and suppression of antitumor immunity. Cell Rep. 2021;35(11):109235.
62.Yang WS, Stockwell BR. Synthetic Lethal Screening Identifies Compounds Activating Iron-Dependent, Nonapoptotic Cell Death in Oncogenic-RAS-Harboring Cancer Cells. Chemistry & Biology. 2008;15(3):234-45.
63.Kuang F, Liu J, Tang D, Kang R. Oxidative Damage and Antioxidant Defense in Ferroptosis. Front Cell Dev Biol. 2020;8:586578-.
64.Dodson M, Castro-Portuguez R, Zhang DD. NRF2 plays a critical role in mitigating lipid peroxidation and ferroptosis. Redox Biol. 2019;23:101107.
65.Doll S, Freitas FP, Shah R, Aldrovandi M, da Silva MC, Ingold I, et al. FSP1 is a glutathione-independent ferroptosis suppressor. Nature. 2019;575(7784):693-8.
66.Bersuker K, Hendricks JM, Li Z, Magtanong L, Ford B, Tang PH, et al. The CoQ oxidoreductase FSP1 acts parallel to GPX4 to inhibit ferroptosis. Nature. 2019;575(7784):688-92.
67.Geng N, Shi BJ, Li SL, Zhong ZY, Li YC, Xua WL, et al. Knockdown of ferroportin accelerates erastin-induced ferroptosis in neuroblastoma cells. European review for medical and pharmacological sciences. 2018;22(12):3826-36.
68.Wang Y, Zhang M, Bi R, Su Y, Quan F, Lin Y, et al. ACSL4 deficiency confers protection against ferroptosis-mediated acute kidney injury. Redox Biology. 2022;51:102262.
69.Doll S, Proneth B, Tyurina YY, Panzilius E, Kobayashi S, Ingold I, et al. ACSL4 dictates ferroptosis sensitivity by shaping cellular lipid composition. Nature Chemical Biology. 2017;13(1):91-8.
70.Drummen GP, Gadella BM, Post JA, Brouwers JF. Mass spectrometric characterization of the oxidation of the fluorescent lipid peroxidation reporter molecule C11-BODIPY(581/591). Free radical biology & medicine. 2004;36(12):1635-44.
71.Drummen GP, van Liebergen LC, Op den Kamp JA, Post JA. C11-BODIPY(581/591), an oxidation-sensitive fluorescent lipid peroxidation probe: (micro)spectroscopic characterization and validation of methodology. Free radical biology & medicine. 2002;33(4):473-90.
72.Hou W, Xie Y, Song X, Sun X, Lotze MT, Zeh HJ, et al. Autophagy promotes ferroptosis by degradation of ferritin. Autophagy. 2016;12(8):1425-8.
73.Wang Y, Tang M. PM2.5 induces ferroptosis in human endothelial cells through iron overload and redox imbalance. Environmental Pollution. 2019;254:112937.
74.Fujimaki M, Furuya N, Saiki S, Amo T, Imamichi Y, Hattori N. Iron Supply via NCOA4-Mediated Ferritin Degradation Maintains Mitochondrial Functions. Mol Cell Biol. 2019;39(14):e00010-19.
75.Issitt T, Bosseboeuf E, De Winter N, Dufton N, Gestri G, Senatore V, et al. Neuropilin-1 Controls Endothelial Homeostasis by Regulating Mitochondrial Function and Iron-Dependent Oxidative Stress. iScience. 2019;11:205-23.
76.Mon EE, Wei F-Y, Ahmad RNR, Yamamoto T, Moroishi T, Tomizawa K. Regulation of mitochondrial iron homeostasis by sideroflexin 2. J Physiol Sci. 2019;69(2):359-73.
77.Yan H-f, Zou T, Tuo Q-z, Xu S, Li H, Belaidi AA, et al. Ferroptosis: mechanisms and links with diseases. Signal Transduction and Targeted Therapy. 2021;6(1):49.

78.Yao X, Zhang Y, Hao J, Duan H-Q, Zhao C-X, Sun C, et al. Deferoxamine promotes recovery of traumatic spinal cord injury by inhibiting ferroptosis. Neural Regen Res. 2019;14(3):532-41.
79.Zhang Y, Fan B-Y, Pang Y-L, Shen W-Y, Wang X, Zhao C-X, et al. Neuroprotective effect of deferoxamine on erastininduced ferroptosis in primary cortical neurons. Neural Regen Res. 2020;15(8):1539-45.
80.Dixon SJ, Lemberg KM, Lamprecht MR, Skouta R, Zaitsev EM, Gleason CE, et al. Ferroptosis: an iron-dependent form of nonapoptotic cell death. Cell. 2012;149(5):1060-72.
81.Sui X, Zhang R, Liu S, Duan T, Zhai L, Zhang M, et al. RSL3 Drives Ferroptosis Through GPX4 Inactivation and ROS Production in Colorectal Cancer. Front Pharmacol. 2018;9:1371-.
82.Bai Y, Meng L, Han L, Jia Y, Zhao Y, Gao H, et al. Lipid storage and lipophagy regulates ferroptosis. Biochemical and Biophysical Research Communications. 2019;508(4):997-1003.
83.Liang D, Minikes AM, Jiang X. Ferroptosis at the intersection of lipid metabolism and cellular signaling. Molecular Cell. 2022;82(12):2215-27.
84.Dong B, Song W, Lu Y, Sun Y, Lin W. Revealing the Viscosity Changes in Lipid Droplets during Ferroptosis by the Real-Time and In Situ Near-Infrared Imaging. ACS Sensors. 2021;6(1):22-6.
85.Finazzi D, Arosio P. Biology of ferritin in mammals: an update on iron storage, oxidative damage and neurodegeneration. Archives of Toxicology. 2014;88(10):1787-802.
86.Liu J, Kuang F, Kroemer G, Klionsky DJ, Kang R, Tang D. Autophagy-Dependent Ferroptosis: Machinery and Regulation. Cell chemical biology. 2020;27(4):420-35.
87.Levi S, Corsi B, Bosisio M, Invernizzi R, Volz A, Sanford D, et al. A Human Mitochondrial Ferritin Encoded by an Intronless Gene*. Journal of Biological Chemistry. 2001;276(27):24437-40.
88.Nie G, Sheftel AD, Kim SF, Ponka P. Overexpression of mitochondrial ferritin causes cytosolic iron depletion and changes cellular iron homeostasis. Blood. 2005;105(5):2161-7.
89.Wang Y-Q, Chang S-Y, Wu Q, Gou Y-J, Jia L, Cui Y-M, et al. The Protective Role of Mitochondrial Ferritin on Erastin-Induced Ferroptosis. 2016;8(308).
90.Yang H, Yang M, Guan H, Liu Z, Zhao S, Takeuchi S, et al. Mitochondrial ferritin in neurodegenerative diseases. Neuroscience research. 2013;77(1-2):1-7.
91.Gao G, Chang Y-Z. Mitochondrial ferritin in the regulation of brain iron homeostasis and neurodegenerative diseases. 2014;5(19).
92.Kudriavtseva AV, Anedchenko EA, Oparina N, Krasnov GS, Kashkin KN, Dmitriev AA, et al. [Expression of FTL and FTH genes encoding ferretin subunits in lung and renal carcinomas]. Molekuliarnaia biologiia. 2009;43(6):1044-54.
93.Tyrrell RM. Activation of mammalian gene expression by the UV component of sunlight--from models to reality. BioEssays : news and reviews in molecular, cellular and developmental biology. 1996;18(2):139-48.
94.Pourzand C, Watkin RD, Brown JE, Tyrrell RM. Ultraviolet A radiation induces immediate release of iron in human primary skin fibroblasts: the role of ferritin. Proc Natl Acad Sci U S A. 1999;96(12):6751-6.
95.Valerio HP, Ravagnani FG, Yaya Candela AP, Dias Carvalho da Costa B, Ronsein GE, Di Mascio P. Spatial proteomics reveals subcellular reorganization in human keratinocytes exposed to UVA light. iScience. 2022;25(4):104093.
96.Jugé R, Breugnot J, Da Silva C, Bordes S, Closs B, Aouacheria A. Quantification and Characterization of UVB-Induced Mitochondrial Fragmentation in Normal Primary Human Keratinocytes. Scientific Reports. 2016;6(1):35065.
97.Hadian K. Ferroptosis Suppressor Protein 1 (FSP1) and Coenzyme Q10 Cooperatively Suppress Ferroptosis. Biochemistry. 2020;59(5):637-8.

98.Riegman M, Sagie L, Galed C, Levin T, Steinberg N, Dixon SJ, et al. Ferroptosis occurs through an osmotic mechanism and propagates independently of cell rupture. Nat Cell Biol. 2020;22(9):1042-8.
99.Xu Z, Wei Y, Gong J, Cho H, Park JK, Sung ER, et al. NRF2 plays a protective role in diabetic retinopathy in mice. Diabetologia. 2014;57(1):204-13.
100.Espinosa-Diez C, Miguel V, Mennerich D, Kietzmann T, Sánchez-Pérez P, Cadenas S, et al. Antioxidant responses and cellular adjustments to oxidative stress. Redox Biol. 2015;6:183-97.
101.Kerins MJ, Ooi A. The Roles of NRF2 in Modulating Cellular Iron Homeostasis. Antioxidants & redox signaling. 2018;29(17):1756-73.
102.Fan Z, Wirth AK, Chen D, Wruck CJ, Rauh M, Buchfelder M, et al. Nrf2-Keap1 pathway promotes cell proliferation and diminishes ferroptosis. Oncogenesis. 2017;6(8):e371.
103.Ishii T, Itoh K, Takahashi S, Sato H, Yanagawa T, Katoh Y, et al. Transcription factor Nrf2 coordinately regulates a group of oxidative stress-inducible genes in macrophages. The Journal of biological chemistry. 2000;275(21):16023-9.
104.Lu S, Song Y, Luo R, Li S, Li G, Wang K, et al. Ferroportin-Dependent Iron Homeostasis Protects against Oxidative Stress-Induced Nucleus Pulposus Cell Ferroptosis and Ameliorates Intervertebral Disc Degeneration In Vivo. Oxid Med Cell Longev. 2021;2021:6670497.
105.Ward DM, Kaplan J. Ferroportin-mediated iron transport: expression and regulation. Biochimica et biophysica acta. 2012;1823(9):1426-33.
106.Harada N, Kanayama M, Maruyama A, Yoshida A, Tazumi K, Hosoya T, et al. Nrf2 regulates ferroportin 1-mediated iron efflux and counteracts lipopolysaccharide-induced ferroportin 1 mRNA suppression in macrophages. Archives of biochemistry and biophysics. 2011;508(1):101-9.
107.Gain P, Jullienne R, He Z, Aldossary M, Acquart S, Cognasse F, et al. Global Survey of Corneal Transplantation and Eye Banking. JAMA Ophthalmol. 2016;134(2):167-73.
108.Vile GF, Tyrrell RM. UVA radiation-induced oxidative damage to lipids and proteins in vitro and in human skin fibroblasts is dependent on iron and singlet oxygen. Free radical biology & medicine. 1995;18(4):721-30.
109.Morlière P, Moysan A, Santus R, Hüppe G, Mazière JC, Dubertret L. UVA-induced lipid peroxidation in cultured human fibroblasts. Biochim Biophys Acta. 1991;1084(3):261-8.
110.Punnonen K, Jansén CT, Puntala A, Ahotupa M. Effects of in vitro UVA irradiation and PUVA treatment on membrane fatty acids and activities of antioxidant enzymes in human keratinocytes. The Journal of investigative dermatology. 1991;96(2):255-9.
111.Doll S, Freitas FP, Shah R, Aldrovandi M, da Silva MC, Ingold I, et al. FSP1 is a glutathione-independent ferroptosis suppressor. Nature. 2019;575(7784):693-8.

List of abbreviations

DFO: Deferoxamine

DHE: Dihydroethidium

EDM: Endothelial cell-Descemet membrane

FASP: Filter assisted sample preparation

FECD: Fuchs endothelial corneal dystrophy

ILEB: Iowa Lions Eye Bank

IRB: Institutional Review Board

LDH: Lactate dehydrogenase

MudPIT: Multidimensional protein identification technology

NAC: N-Acetylcysteine

NGF: Nerve growth factor

ROS: Reactive oxygen species

SEM: Standard error of the mean

TFRA: transferrin receptor 1

USP: United States Pharmacopeia

UVA: Ultraviolet A

Figure Legends

Figure 1: FECD surgical tissues show key markers of ferroptosis. (A) 4-HNE protein expressions in human surgical samples from patients with FECD. **(B)** Cytosolic Fe^{2+} in primary endothelial cells isolated from healthy human donor corneas (n = 12) and FECD corneas (n = 7). Data are shown as mean±SEM; **p < 0.01, Student's t-test. **(C)** GPX4 mRNA expression in FECD and control human tissues. **(D)** SOD2 mRNA and protein expression in FECD and control tissues. (**E**) NRF2 mRNA and protein expression in FECD and control tissues. (**F**) FSP1 mRNA and protein expression in FECD and control tissues. (**G**) Ferroportin mRNA and protein expression in FECD and control tissues. (**H**) ACSL4 mRNA expression in FECD and control tissues. All data of mRNA and protein expression are shown as mean±SEM for n = 4 (Control tissues) and n = 8 (FECD tissues). All the statistical comparisons were conducted using two-tailed, unpaired Student's t-test, *p < 0.05, **p < 0.01, ****p < 0.0001. Relative gene expression is normalized by *β*-actin. (**I**) Heatmap with hierarchical clustering for 211 genes from the FerrDB database that includes all driver, suppressor and marker ferroptosis genes that were expressed in the RNA-Seq datasets. For each plot, "pearson" was used for the clustering distance and "complete" for the hierarchical clustering method. The location where the representative dataset was collected (Mayo, Russia, or UTSW) and mutation type (Control, no TCF4 repeats [No_Rep] or TCF repeats [TCF4_Rep]) are shown for each sample.

Figure 2: FECD cell culture model shows key marker of ferroptosis. (A) 4-HNE protein expressions in HCEC-B4G12 and F35T cells. (**B**) Basal level of lipid peroxidation in HCEC-B4G12 and F35T cells quantified by C11-BODIPY fluorescent probe using flow cytometer. Comparisons of median fluorescence of C11-BODIPY detected in HCEC-B4G12 and F35T cells (10000 cells). Data are shown as mean±SEM; n = 3; ****p < 0.0001, Student's t-test. C11-BODIPY (FL1 fluorescence) peak of F35T cells shifts to right when compares to B4G12

cells. (**C**) Representative confocal images showing fluorescence of reduced and oxidized dye in the indicated cell lines. (**D**) Representation of median of the fluorescence of FerroOrange showing significant difference in cytosolic Fe^{2+} between indicated cells. B4G12 and F35T cells were stained with FerroOrange fluorescent probe to quantify cytosolic Fe^{2+} by flow cytometer. A minimum ten thousand cells were quantified for measuring the fluorescence. **(E)** Cell population distribution after staining with FerroOrange showing cytosolic Fe^{2+} content. **(F)** Representation of confocal microscopy images of HCEC-B4G12 and F35T cells stained with FerroOrange fluorescent probe showing and comparing cytosolic Fe^{2+}. **(G)** Representation of median of the fluorescence of Mito-FerroGreen showing significant difference in mitochondrial Fe^{2+} between indicated cells. HCEC-B4G12 and F35T cells were stained with Mito-FerroGreen fluorescent probe to quantify mitochondrial Fe^{2+} by flow cytometer. A minimum ten thousand cells were quantified for measuring the fluorescence. **(H)** Cell population distribution after staining with Mito-FerroGreen showing mitochondrial Fe^{2+} content. **(I)** Representation of confocal microscopy images of HCEC-B4G12 and F35T cells stained with Mito-FerroGreen fluorescent probe showing and comparing mitochondrial Fe^{2+}. Data are represented as means ± SEM; n = 3; unpaired Student's t-test, ****$p < 0.0001$. **(J)** Deferoxamine (DFO) iron chelation assay where HCEC-B4G12 and F35T cells were treated with DFO for 24h and then challenged with RSL3 at 1, 2 and 5 μM for different durations of 2, 4, 6 and 8h. Cell viability was measured by MTS assay. Data are represented as means ± SEM for three biological replicates; Student's t-test, * $p < 0.05$, ** $p < 0.01$, *** $p < 0.001$, **** $p < 0.0001$. **(K)** GPX4 mRNA and protein expression in the indicated cells. **(D)** SOD2 mRNA and protein expression in the indicated cells. (**E**) NRF2 mRNA and protein expression in the indicated cells. (**F**) FSP1 mRNA and protein expression in the indicated cells. (**G**) Ferroportin mRNA expression in the indicated cells. (**H**) ACSL4 mRNA expression in the indicated cells. All data of mRNA and protein expression are shown as mean±SEM for n = 5-

9 (B4G12) and n = 5-7 (F35T). All the statistical comparisons were conducted using two-tailed, unpaired Student's t-test, **p < 0.01, ***p < 0.001. Relative gene expression is normalized by *β*-actin.

Figure 3: Expression of TFR1, reactive oxygen species (ROS) and lipid droplets in FECD. **(A)** TFR1 mRNA and protein expression in control and FECD surgical tissues. (**B**) TFR1 mRNA and protein expression in HCEC-B4G12 and F35T cells. Relative gene expression is normalized by β-actin. Data are represented as means ± SEM for n = 4 (Control tissues), n = 8 (FECD tissues), n = 5-9 (B4G12) and n = 5-7 (F35T); unpaired Student's t-test, *p < 0.05, **p < 0.01, ***p < 0.001. **(C)** Mitochondrial ROS quantified by MitoROS 580 dye in the indicated cells. Data are shown as mean±SEM; n = 3; ****p < 0.0001, one-way ANOVA, followed by Tukey's post-hoc test. **(D)** Representation of median of the fluorescence of DHE showing significant difference in ROS between indicated cells. DHE (FL2 fluorescence) peak of F35T cells shifts to right when compares to B4G12 cells. **(E)** Representative confocal images showing fluorescence of DHE indicating ROS in the indicated cell lines. **(F)** Representation of median of the fluorescence of LipidSpot™ 610 showing significant difference in ROS between indicated cells. LipidSpot™ 610 (FL4 fluorescence) peak of F35T cells shifts to right when compares to B4G12 cells. **(G)** Representative confocal images showing fluorescence of LipidSpot™ 610 indicating lipid droplets in the indicated cell lines. In flow cytometer analysis, data are shown as mean±SEM; n = 9 (3 biological replicates × 3 technical replicates); ****p < 0.0001, Student's t-test.

Figure 4: FECD demonstrates iron overload associated with decreased ferritin and UVA irradiation. **(A)** Representation of cellular iron metabolism in ferroptosis process. **(B)** Quantification of human ferritin (Ft) by ELISA in protein from HCEC-B4G12 and F35T cells.

The human ferritin levels are presented as mean±SEM; n = 9 (3 biological replicates × 3 technical replicates); ***p <0.001, Student's t-test. **(C)** Quantification of mitochondrial ferritin (FtMt) by ELISA in protein from HCEC-B4G12 and F35T cells. The mitochondrial ferritin levels are presented as mean±SEM; n = 9 (3 biological replicates × 3 technical replicates); ****p < 0.0001, Student's t-test. **(D)** FTH mRNA expression in control and FECD tissues. **(E)** FTL mRNA expression in control and FECD tissues. **(F)** FTH mRNA expression in indicated cells. **(G)** FTL mRNA expression in indicated cells. All data of mRNA expression are shown as mean±SEM for n = 4 (Control tissues), n = 8 (FECD tissues), n = 7-9 (B4G12) and n = 6-7 (F35T). All the statistical comparisons were conducted using two-tailed, unpaired Student's t-test, *p < 0.05, **p < 0.01, ***p < 0.001. Relative gene expression is normalized by β-actin. **(H)** Cytosolic Fe^{2+} release in human donor corneas upon UVA irradiation at 5 J/cm^2. Primary endothelial cells were isolated after UVA irradiation and stained with FerroOrange fluorescent probe. The experiment was conducted pairwise, where the left cornea was used as control and the right cornea was exposed to UVA. **(I)** Comparison of geometric mean of FerroOrange (FL2 fluorescence) signals. Data are mean±SEM, Paired two-tailed Student's t-test. **(J)** Representation of percent increase of labile cytosolic Fe^{2+} after UVA irradiation at the fluence of 1, 2, 4 and 8 J/cm^2. Indicated cells were stained with FerroOrange fluorescent probe immediately post-UVA (Data are shown as mean±SEM, n = 9; 3 biological replicates × 3 technical replicates; ***p < 0.001, ****p < 0.0001, one-way ANOVA, followed by Tukey's post-hoc test). **(K)** Representation of percent increase of mitochondrial Fe^{2+} after UVA irradiation at the fluence of 1, 2, 4 and 8 J/cm^2. Indicated cells were stained with Mito-FerroGreen fluorescent probe immediately post-UVA (Data are shown as mean±SEM, n = 9; 3 biological replicates × 3 technical replicates; ****p < 0.0001, one-way ANOVA, followed by Tukey's post-hoc test.).

Figure 5: Solubilized ubiquinol gives protection against lipid peroxidation. (A) Schematic showing RSL3 induced ferroptosis process and role of solubilized ubiquinol to prevent lipid peroxidation and ferroptosis. **(B)** Solubilized ubiquinol prevent lipid peroxidation in HCEC-B4G12 and F35T cells induced by RSL3 in concertation dependent manner detected by the peak shift of C11-BODPY fluorescent probe in flow cytometer analysis. **(C)** C11-BODIPY fluorescence signals detected by flow cytometer following treatments with solubilized ubiquinol at different concentrations of 1, 10, 50 and 100 μM. Values are mean±SEM; n = 3; ****p <0.0001, Student's t-test against RSL3-untreated group. **(D)** Representation of cell population undergoing RSL3 induced lipid peroxidation following solubilized ubiquinol treatment at the indicated concentrations in HCEC-B4G12 and F35T cells. Solubilized ubiquinol decreased the number of cells undergoing lipid peroxidation at concentration dependent manner. Values are mean±SEM; n = 3.

Figure 6: Solubilized ubiquinol gives protection against ferroptosis. (A) Cell viability assay by quantifying LDH release after treatments with solubilized ubiquinol at different concentrations of 1, 5, 10, 50, and 100 μM. Following solubilized ubiquinol treatment HCEC-B4G12 and F35T cells were challenged with 1 μM of RSL3 for 24 h. Data are shown as mean±SEM; n = 3; ****p < 0.0001, Student's t-test against RSL3 alone group. **(B)** Comparisons of cell viability of HCEC-B4G12 and F35T cells following the treatment of solubilized ubiquinol. Solubilized ubiquinol was comparatively less effective in F35T cells indication more ferroptosis than in B4G12 cells. Data are shown as mean±SEM; n = 3; *p < 0.05, **p < 0.01, **** p < 0.0001, Student's t-test. **(C)** Representative light microscopy images showing solubilized ubiquinol at 1 μM dose inhibited RSL3 induced ferroptosis in HCEC-B4G12 and F35T cells. **(D)** Representative confocal images showing RSL3 induced lipid droplets in the indicated cells. **(E)** Representative confocal images showing disappearance of

lipid droplets at the time of ferroptosis induced death in the indicated cells. SYTOX green indicates cell death. **(F)** Solubilized ubiquinol outperforms NAC, DFO and ferrostatin-1 in protecting F35T cells against RSL3 induced cell death in ferroptosis assay. Data are shown as mean±SEM, n = 3; **** $p < 0.0001$, Student's t-test.

Figure 7: Summary of molecular mechanism of ferroptosis in FECD. Iron gets into cell in ferric form using TFR1 mediated endocytosis. Ferritin stores the excess iron in ferric form which is nontoxic. Ferric form of iron gets converted to ferrous form in endosome. When labile ferrous form of iron gets released into cytosol, it causes lipid peroxidation via Fenton reactions. UVA irradiation can cause iron release from the ferritin and eventually increases the labile iron in the cytosol and increases iron mediated lipid peroxidation known as ferroptosis. GPX4 is the master regulator of ferroptosis. In this study, RSL3 was used to block GPX4 to induce ferroptosis. Ubiquinol is a potent ferroptosis inhibitor. Other molecules like DFO and artesunate can prevent ferroptosis by quenching labile toxic ferrous iron.

Figure 1:

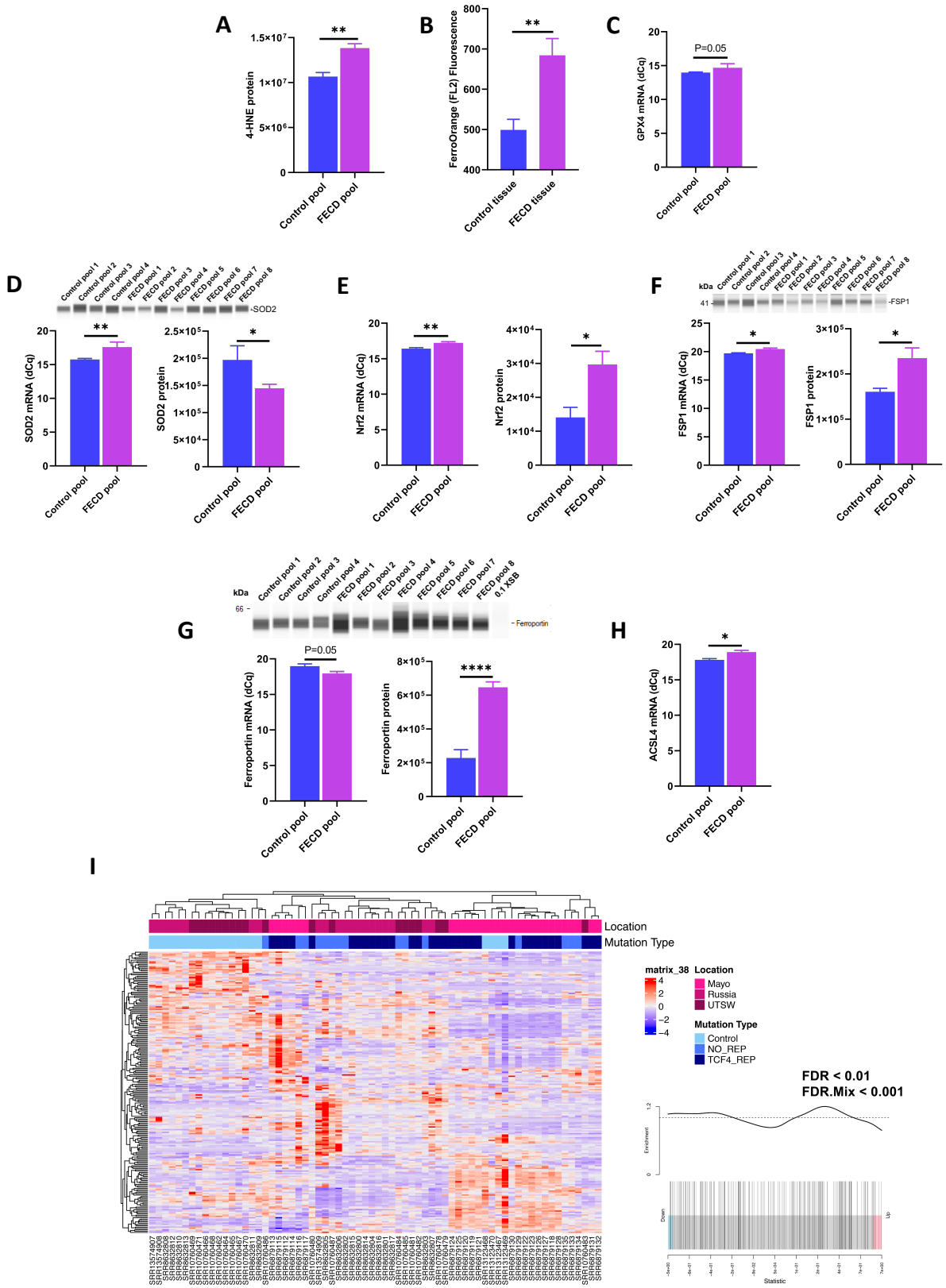
A
4-HNE protein
Control pool
FECD pool
B
FerroOrange (FL2) Fluorescence
Control tissue
FECD tissue
C
GPX4 mRNA (dCq)
P=0.05
D
SOD2
SOD2 mRNA (dCq)
SOD2 protein
E
Nrf2 mRNA (dCq)
Nrf2 protein
F
FSP1
FSP1 mRNA (dCq)
FSP1 protein
G
Ferroportin
Ferroportin mRNA (dCq)
Ferroportin protein
H
ACSL4 mRNA (dCq)
I
Location
Mutation Type
matrix_38
Mayo
Russia
UTSW
Control
NO_REP
TCF4_REP
FDR < 0.01
FDR.Mix < 0.001
Enrichment
Statistic

Figure 2:

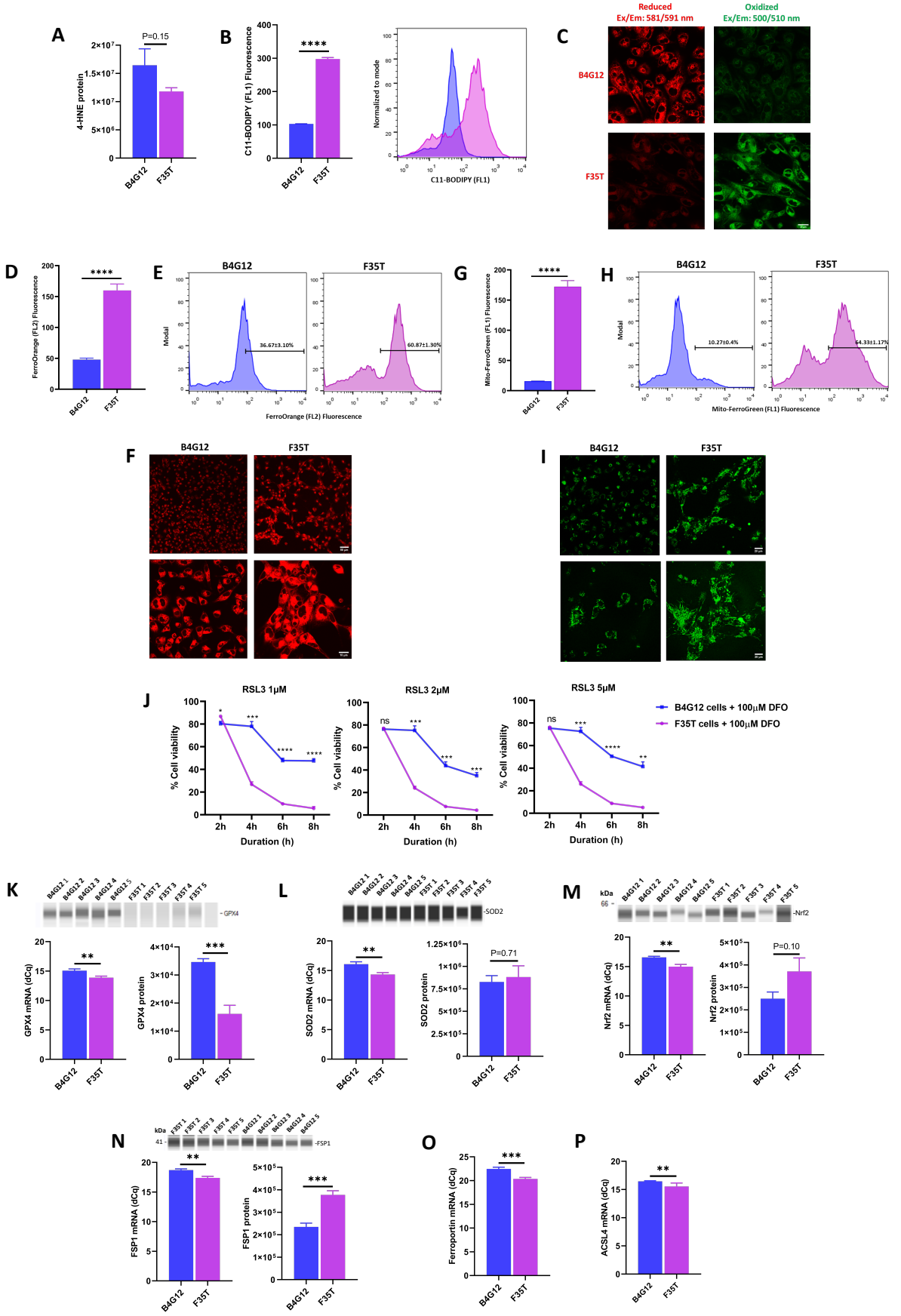
A
P=0.15
4-HNE protein
B4G12
F35T
B
****
C11-BODIPY (FL1) Fluorescence
Normalized to mode
C11-BODIPY (FL1)
C
Reduced
Ex/Em: 581/591 nm
Oxidized
Ex/Em: 500/510 nm
B4G12
F35T
D
****
FerroOrange (FL2) Fluorescence
E
B4G12
F35T
36.67±3.10%
60.87±1.30%
Modal
FerroOrange (FL2) Fluorescence
G
****
Mito-FerroGreen (FL1) Fluorescence
H
B4G12
F35T
10.27±0.4%
64.33±1.17%
Modal
Mito-FerroGreen (FL1) Fluorescence
F
B4G12
F35T
I
B4G12
F35T
J
RSL3 1μM
RSL3 2μM
RSL3 5μM
% Cell viability
Duration (h)
B4G12 cells + 100μM DFO
F35T cells + 100μM DFO
K
GPX4
GPX4 mRNA (dCq)
GPX4 protein
L
SOD2
SOD2 mRNA (dCq)
SOD2 protein
P=0.71
M
Nrf2
Nrf2 mRNA (dCq)
Nrf2 protein
P=0.10
N
FSP1
FSP1 mRNA (dCq)
FSP1 protein
O
Ferroportin mRNA (dCq)
P
ACSL4 mRNA (dCq)

Figure 3:

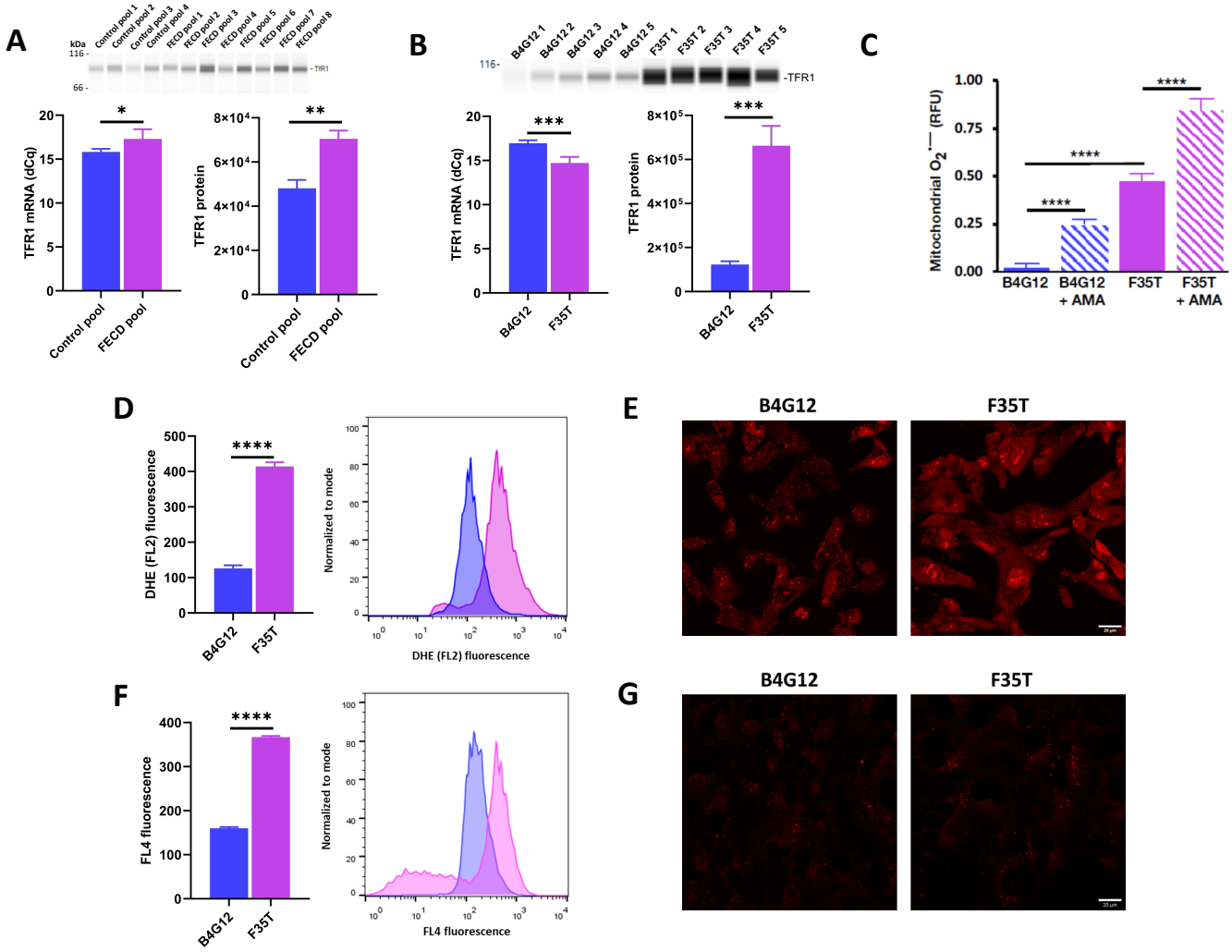
A
kDa
116 -
66 -
Control pool 1
Control pool 2
Control pool 3
Control pool 4
FECD pool 1
FECD pool 2
FECD pool 3
FECD pool 4
FECD pool 5
FECD pool 6
FECD pool 7
FECD pool 8
- TfR1
TFR1 mRNA (dCq)
TFR1 protein
Control pool
FECD pool
B
116-
B4G12 1
B4G12 2
B4G12 3
B4G12 4
B4G12 5
F35T 1
F35T 2
F35T 3
F35T 4
F35T 5
-TFR1
B4G12
F35T
C
Mitochondrial O2•− (RFU)
B4G12
B4G12 + AMA
F35T
F35T + AMA
D
DHE (FL2) fluorescence
Normalized to mode
E
B4G12
F35T
F
FL4 fluorescence
G

Figure 4

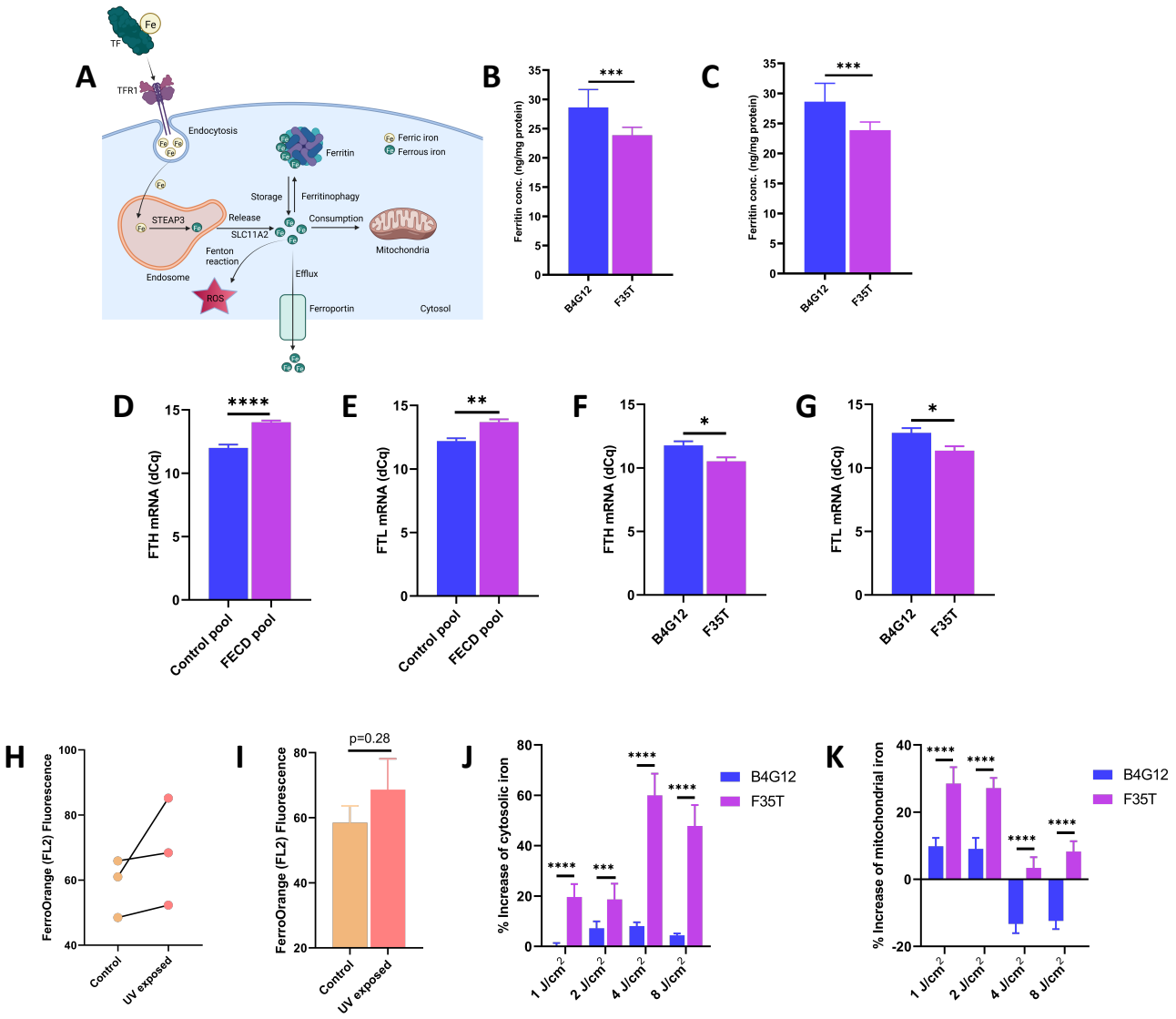
A
TF
Fe
TFR1
Endocytosis
Ferritin
Ferric iron
Ferrous iron
Storage
Ferritinophagy
STEAP3
Release
SLC11A2
Consumption
Mitochondria
Fenton reaction
Endosome
ROS
Efflux
Ferroportin
Cytosol
B
Ferritin conc. (ng/mg protein)
***
B4G12
F35T
C
Ferritin conc. (ng/mg protein)
***
B4G12
F35T
D
FTH mRNA (dCq)
****
Control pool
FECD pool
E
FTL mRNA (dCq)
**
Control pool
FECD pool
F
FTH mRNA (dCq)
*
B4G12
F35T
G
FTL mRNA (dCq)
*
B4G12
F35T
H
FerroOrange (FL2) Fluorescence
Control
UV exposed
I
FerroOrange (FL2) Fluorescence
p=0.28
Control
UV exposed
J
% Increase of cytosolic iron
B4G12
F35T
****
***
****
****
1 J/cm2
2 J/cm2
4 J/cm2
8 J/cm2
K
% Increase of mitochondrial iron
B4G12
F35T
****
****
****
****
1 J/cm2
2 J/cm2
4 J/cm2
8 J/cm2

Figure 5:

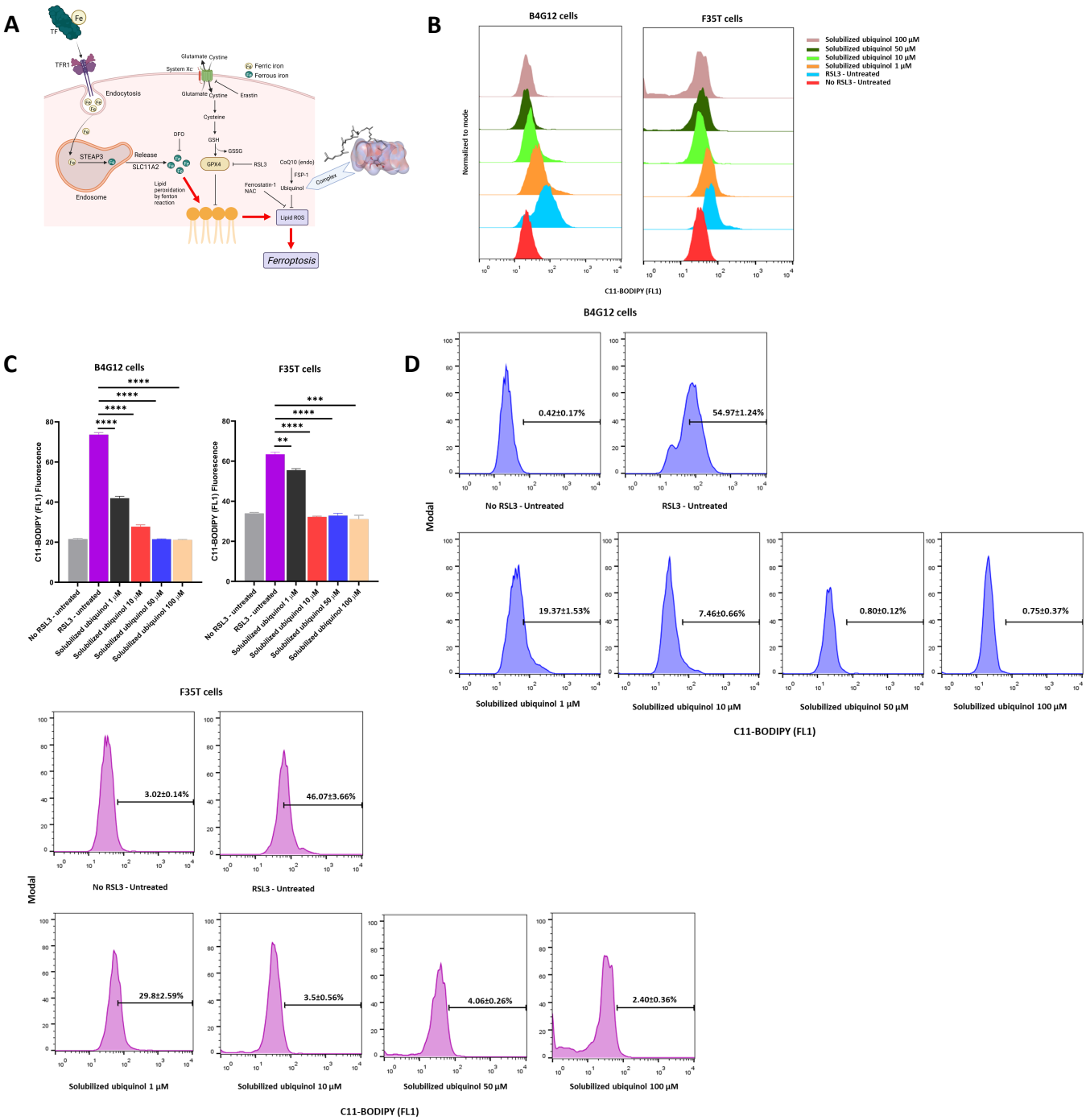
A
TF
TFR1
Endocytosis
Endosome
STEAP3
Release
SLC11A2
Lipid peroxidation by fenton reaction
Glutamate Cystine
System Xc
Ferric iron
Ferrous iron
Erastin
Cysteine
DFO
GSH
GSSG
GPX4
RSL3
CoQ10 (endo)
FSP-1
Ferrostatin-1 NAC
Ubiquinol
Complex
Lipid ROS
Ferroptosis
B
B4G12 cells
F35T cells
Normalized to mode
Solubilized ubiquinol 100 µM
Solubilized ubiquinol 50 µM
Solubilized ubiquinol 10 µM
Solubilized ubiquinol 1 µM
RSL3 - Untreated
No RSL3 - Untreated
C11-BODIPY (FL1)
C
B4G12 cells
F35T cells
C11-BODIPY (FL1) Fluorescence
No RSL3 - untreated
RSL3 - untreated
Solubilized ubiquinol 1 µM
Solubilized ubiquinol 10 µM
Solubilized ubiquinol 50 µM
Solubilized ubiquinol 100 µM
D
B4G12 cells
0.42±0.17%
54.97±1.24%
No RSL3 - Untreated
RSL3 - Untreated
Modal
19.37±1.53%
7.46±0.66%
0.80±0.12%
0.75±0.37%
Solubilized ubiquinol 1 µM
Solubilized ubiquinol 10 µM
Solubilized ubiquinol 50 µM
Solubilized ubiquinol 100 µM
C11-BODIPY (FL1)
F35T cells
3.02±0.14%
46.07±3.66%
No RSL3 - Untreated
RSL3 - Untreated
Modal
29.8±2.59%
3.5±0.56%
4.06±0.26%
2.40±0.36%
Solubilized ubiquinol 1 µM
Solubilized ubiquinol 10 µM
Solubilized ubiquinol 50 µM
Solubilized ubiquinol 100 µM
C11-BODIPY (FL1)

Figure 6:

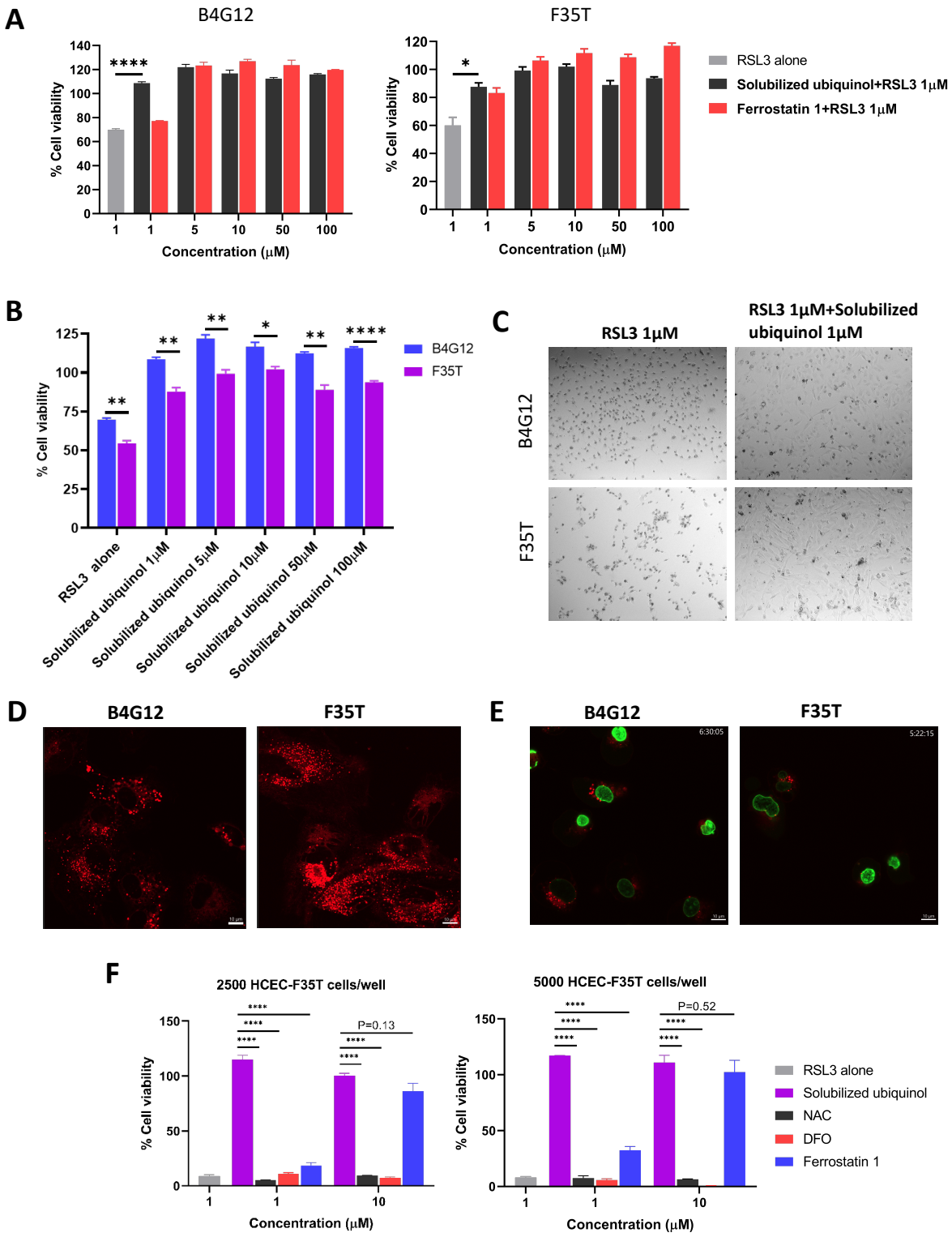
A
B4G12
F35T
% Cell viability
Concentration (µM)
RSL3 alone
Solubilized ubiquinol+RSL3 1µM
Ferrostatin 1+RSL3 1µM
B
B4G12
F35T
RSL3 alone
Solubilized ubiquinol 1µM
Solubilized ubiquinol 5µM
Solubilized ubiquinol 10µM
Solubilized ubiquinol 50µM
Solubilized ubiquinol 100µM
C
RSL3 1µM
RSL3 1µM+Solubilized ubiquinol 1µM
D
E
F
2500 HCEC-F35T cells/well
5000 HCEC-F35T cells/well
P=0.13
P=0.52
NAC
DFO
Ferrostatin 1

Figure 7:

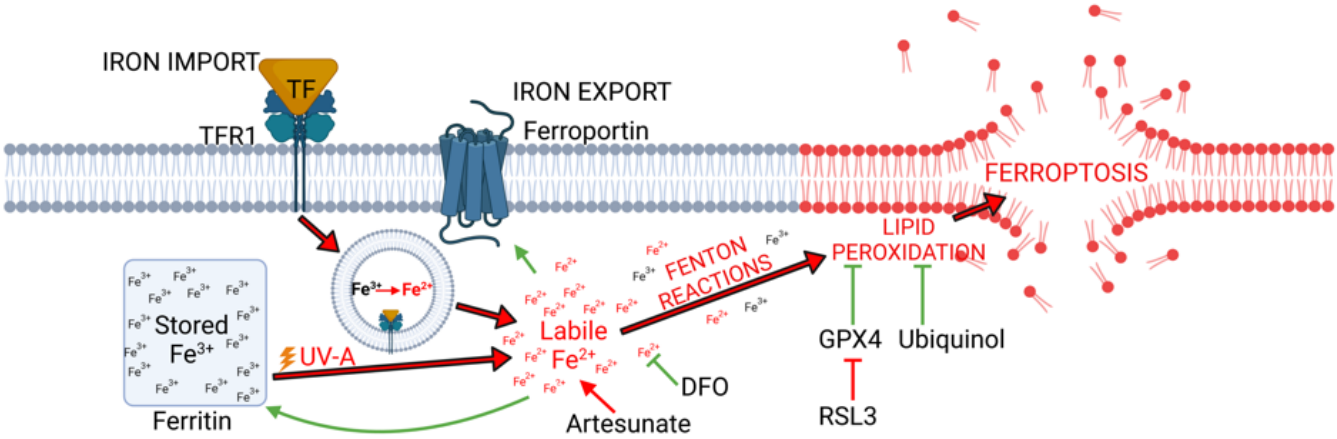
IRON IMPORT
TF
TFR1
IRON EXPORT
Ferroportin
FERROPTOSIS
LIPID
PEROXIDATION
FENTON
REACTIONS
Stored
Fe3+
Ferritin
UV-A
Labile
Fe2+
DFO
Artesunate
GPX4
Ubiquinol
RSL3